Water Resources Research

RESEARCH ARTICLE
10.1029/2019WR024815

Special Section:
Advancing process representation in hydrologic models: Integrating new concepts, knowledge, and data

Quantifying the Controls on Evapotranspiration Partitioning in the Highest Alpine Meadow Ecosystem

Jiangpeng Cui[1,2], Lide Tian[3], Zhongwang Wei[4,5], Chris Huntingford[6], Pei Wang[7], Zhongyin Cai[3], Ning Ma[1], and Lixin Wang[8]

[1]Key Laboratory of Tibetan Plateau Environment Change and Land Surface Processes, Institute of Tibetan Plateau Research, Chinese Academy of Sciences, Beijing, China, [2]Sino-French Institute for Earth System Science, College of Urban and Environmental Sciences, Peking University, Beijing, China, [3]Institute of International Rivers and Eco-Security, Yunnan University, Kunming, China, [4]Southern Marine Science and Engineering Guangdong Laboratory (Zhuhai), Guangdong Province Key Laboratory for Climate Change and Natural Disaster Studies, School of Atmospheric Sciences, Sun Yat-sen University, Guangzhou, China, [5]Chiba Experiment Station of Institute of Industrial Science, The University of Tokyo, Chiba, Japan, [6]Centre for Ecology and Hydrology, Wallingford, UK, [7]State Key Laboratory of Earth Surface Processes and Resource Ecology, Faculty of Geographical Science, Beijing Normal University, Beijing, China, [8]Department of Earth Sciences, Indiana University-Purdue University Indianapolis, Indianapolis, IN, USA

Key Points:
- Laser spectroscopy and the chamber method were used to estimate T/ET in the central Tibetan Plateau
- Near-surface soil water content dominated the temporal change of T/ET, with leaf area index playing a secondary role
- Our study highlights the critical impact of environmental conditions on the temporal change of T/ET in water-limited regions

Supporting Information:
- Supporting Information S1

Correspondence to:
J. Cui and L. Tian,
cuijp@pku.edu.cn;
ldtian@ynu.edu.cn

Citation:
Cui, J., Tian, L., Wei, Z., Huntingford, C., Wang, P., Cai, Z., et al (2020). Quantifying the controls on evapotranspiration partitioning in the highest alpine meadow ecosystem. *Water Resources Research*, *55*. https://doi.org/10.1029/2019WR024815

Received 21 JAN 2019
Accepted 14 MAR 2020
Accepted article online 17 MAR 2020

Abstract Quantifying the transpiration fraction of evapotranspiration (T/ET) is crucial for understanding plant functionality in ecosystem water cycles, land-atmosphere interactions, and the global water budget. However, the controls and mechanisms underlying the temporal change of T/ET remain poorly understood in arid and semiarid areas, especially for remote regions with sparse observations such as the Tibetan Plateau (TP). In this study, we used combined high-frequency laser spectroscopy and chamber methods to constrain estimates of T/ET for an alpine meadow ecosystem in the central TP. The three isotopic end members in ET (δ_{ET}), soil evaporation (δ_E), and plant transpiration (δ_T) were directly determined by three newly customized chambers. Results showed that the seasonal variations of δ_{ET}, δ_E, and δ_T were strongly affected by the precipitation isotope ($R^2 = 0.53$). The $\delta^{18}O$-based T/ET agreed with that of δ^2H. Isotope-based T/ET ranged from 0.15 to 0.73 during the periods of observation, with an average of 0.43. This mean result was supported by T/ET derived from a two-source model and eddy covariance observations. Our overarching finding is that at the seasonal timescale, surface soil water content (θ) dominated the change of T/ET, with leaf area index playing only a secondary role. Our study confirms the critical impact of soil water on the temporal change of T/ET in water-limited regions such as the TP. This knowledge sheds light on diverse land-surface processes, global hydrological cycles, and their modeling.

1. Introduction

Evapotranspiration (ET), consisting principally of plant transpiration (T) and soil evaporation (E), exerts a strong control on terrestrial water cycles (Wang & Dickinson, 2012). Quantifying the ratio between T and ET (T/ET) is important to understand ecological and hydrological processes and their linkages (Lian et al., 2018; Schlesinger & Jasechko, 2014; Wang et al., 2014; Wei et al., 2017). Knowledge of T/ET also guides better understanding of plant and ecosystem water-use efficiency (Good et al., 2014; Hu et al., 2008; Jasechko et al., 2013) and the modeling of plant feedback in response to climate change (Wang et al., 2013). Furthermore, the better representation of plant transpiration within earth system models has been demonstrated to improve the simulations of climate and the global water cycle (Lian et al., 2018).

Although ET partitioning has been evaluated using multiple methods across different ecosystems, considerable uncertainty still exists and at different spatiotemporal scales. At the global scale, the magnitude of T/ET differs substantially (20–80%) among different methods (Good et al., 2015; Jasechko et al., 2013; Maxwell & Condon, 2016; Miralles et al., 2016; Wei et al., 2017; Zhang et al., 2016). This considerable uncertainty is predominantly because of the lack of plot scale ET partitioning observations at relevant spatiotemporal scales for large-scale T/ET upscaling (Wei et al., 2017), constraint (Lian et al., 2018), and validation (Rigden

et al., 2018). Therefore, quantifying the subcomponents of *ET* in plot scales and understanding the factors controlling *ET* partitioning are essential and urgent. This missing quantification is especially true for the remote high-elevation ecosystem with sparse observations, such as the Tibetan Plateau (TP). High-elevation ecosystems are often characterized by arid or semiarid climates, suggesting that there may be a more pronounced sensitivity of ecosystems to climate change and in particular a vulnerability to climate extremes due to the low vegetation cover and biodiversity. For instance, recent climate change, and including rapidly increasing air temperatures, has already resulted in significant changes to the TP's water cycles (Yang et al., 2011). Furthermore, high-elevation regions are usually the headwater of large rivers that provide fresh water to people, agriculture, and other ecosystems located downstream. Better quantification of the role of plants in high-elevation ecosystems enables more reliable projections of further water cycle changes due to ongoing atmospheric greenhouse gas concentration increases and also aids sustainable water resources management. However, *ET* partitioning using direct observations for the high-elevation ecosystems has been reported much less often (Guo et al., 2017), compared to the better-quantified *ET* estimation (Ma et al., 2015, 2019).

Many measurement methods at the plot scale have been developed for determining *ET* partitioning. These include eddy flux measurements, weighing lysimeters, sap flow meters, water isotope (Xiao et al., 2018), and chamber measurements (Kool et al., 2014; Sun et al., 2019; Sutanto et al., 2014). Measurements suggest that *T*/*ET* varies obviously across different ecosystems, generally decreasing from wet climates to semiarid ecosystems (Schlesinger & Jasechko, 2014). However, the precise controlling factors of *T*/*ET* and their magnitude for different ecosystems remains poorly understood. For example, the leaf area index (LAI) and its changes in growing periods partially predict *T*/*ET* but only accounts for 43% of the variations in this fraction (Wang et al., 2014). By further taking vegetation type into consideration, but still using LAI, this explains 58 ± 17% of *T*/*ET* variation (Wei et al., 2017). To date, most previous studies have been mainly focused on the biological aspects, such as LAI variations, in controlling *T*/*ET* (Berkelhammer et al., 2016; Hu et al., 2009; Wang et al., 2014; Wang et al., 2018; Wang & Yamanaka, 2014; Wei et al., 2015; Wu et al., 2016). Much less emphasis has been placed on assessing the impact of environmental conditions, such as water availability (Liu et al., 2002; Wei et al., 2018). Such understanding is important, as plant transpiration is controlled not only by its physiological response but also by the levels of soil moisture availability. Although global statistics show no significant relationship between *T*/*ET* and annual precipitation (Schlesinger & Jasechko, 2014) or soil water potential (Wang et al., 2014), regionally water may still impact this ratio, as so requires assessment. Impacts are expected in particular in arid and semiarid regions, where water is a limiting factor for plant growth. Determining the environment factors controlling *T*/*ET* changes is needed for better upscaling hydrological cycling to large areas (Wei et al., 2017), as well as land-surface modeling (Ma et al., 2017).

Due to the isotopic fractionation in the process of soil evaporation, the isotopic composition of *E* has distinct differences to that of *T* (Yakir & Sternberg, 2000). These different characteristics make isotopes an especially useful diagnostic tool to quantify *T*/*ET*. In a recent review on *ET* partitioning (Sutanto et al., 2014), the authors discussed the limitations and possible discrepancy sources for isotope versus nonisotope methods in determining *T*/*ET* and suggested that isotope-based *T*/*ET* was consistent with the results from hydrometric methods in the same plants and climatic conditions. Isotope-based *ET* partitioning has already been successfully applied in different ecosystems. These ecosystems include forest (Berkelhammer et al., 2016; Sun et al., 2014; Williams et al., 2004), savanna (Dubbert et al., 2013; Yepez et al., 2003), agriculture (Lu et al., 2017; Wei et al., 2015; Wen et al., 2016), grassland (Good et al., 2014; Hu et al., 2014; Wang et al., 2015), and controlled experiments in a laboratory (Rothfuss et al., 2010; Sutanto et al., 2012; Wang et al., 2010). Three isotopic end members, representing the isotopic compositions of *ET* (δ_{ET}), *E* (δ_E), and *T* (δ_T), need precise quantification to estimate *T*/*ET*. Conventionally, the three end members were determined by isotopic models (Craig & Gordon, 1965; Farquhar & Cernusak, 2005; Keeling, 1958). More recently, an alternative chamber method was developed to measure directly δ_{ET}, δ_E, and δ_T, gaining from the development of high-frequency laser spectroscopy (Dubbert et al., 2013; Wang et al., 2010). The major advantage of the chamber method is that it offers an alternative solution to estimating δ_{ET}, δ_E, or δ_T without the use of complex isotopic models. This method has been successfully applied to cropland (Lu et al., 2017) and grassland ecosystems (Good et al., 2014; Wang et al., 2013). However, its performance in high-elevation and cold ecosystems is still unknown.

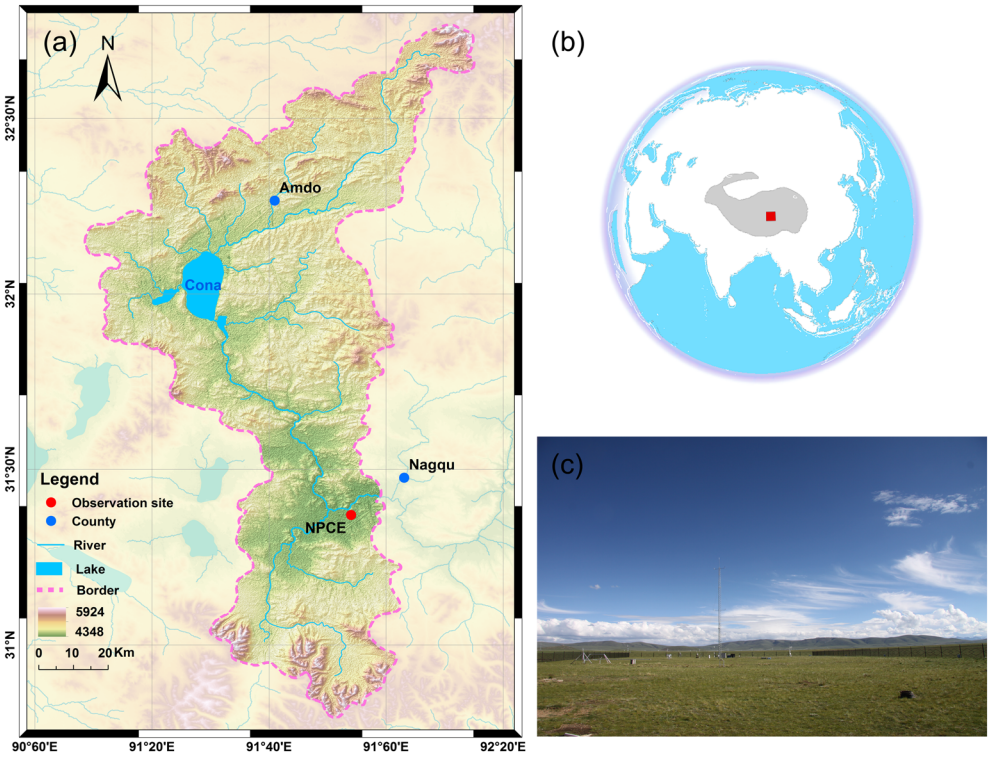

Figure 1. (a) The geographic siting of the Nagqu River Basin, (b) its location (marked by a red rectangle) in the Tibetan Plateau and (c) a photograph of the landscape and in situ flux and meteorology measurement systems in the observational site.

Here we aim to partition *ET* in the central TP using stable water isotopes. We employed a high-frequency laser spectrometry and chamber method in an alpine meadow zone during the growing season. The three end members were directly measured by newly customized chambers (year 2016) or calculated from commonly used nonprocess-based empirical models (Keeling plot, Craig-Gordon (CG) model, and isotopic steady-state assumption, year 2014). Specifically, the objectives of our study are (1) to partition ET into transpiration and evaporation and to investigate how environmental conditions, such as surface soil water content (θ), control the temporal variations of T/ET, in addition to LAI influence, and (2) to evaluate the performance of chamber method and its uncertainties in high-elevation ecosystems, and including any dependence of chamber size, representativeness of chamber coverage and condensation on isotopic values.

2. Materials and Methods

2.1. Site Description

The experiment was conducted at the Nagqu Station of Plateau Climate and Environment, Chinese Academy of Sciences (NPCE, 31°22′N, 91°54′E; 4,509 m above sea level), which is located near to the outlet of the Nagqu River Basin (area 9,498 km^2; Figure 1). The Nagqu River Basin is located on the central TP, with the Nyainqentanglha Mountains to the south and the Tanggula Mountains to the north. The basin also contains the headwaters of the Nujiang-Salween River, with a small lake upstream. This region is characterized by a cold semiarid monsoonal climate ("polar tundra" in the Köppen-Geiger climate classification). Based on a 30-year record (1985–2014) of the Nagqu Meteorological Station located about 20 km to the southwest of NPCE (Figure 1), the mean annual air temperature is −0.4 °C, with monthly averages of −11.3 °C for January and 9.7 °C for July. Mean annual precipitation is 450 mm/year and with 85% of annual precipitation falling during June–September. About 30% of annual precipitation falls as snow in winter and spring.

The geomorphology around the NPCE is overall homogeneous, with a fetch of >2 km in the direction of the prevailing wind and is surrounded by small hills with heights less than 100 m above the mean landscape

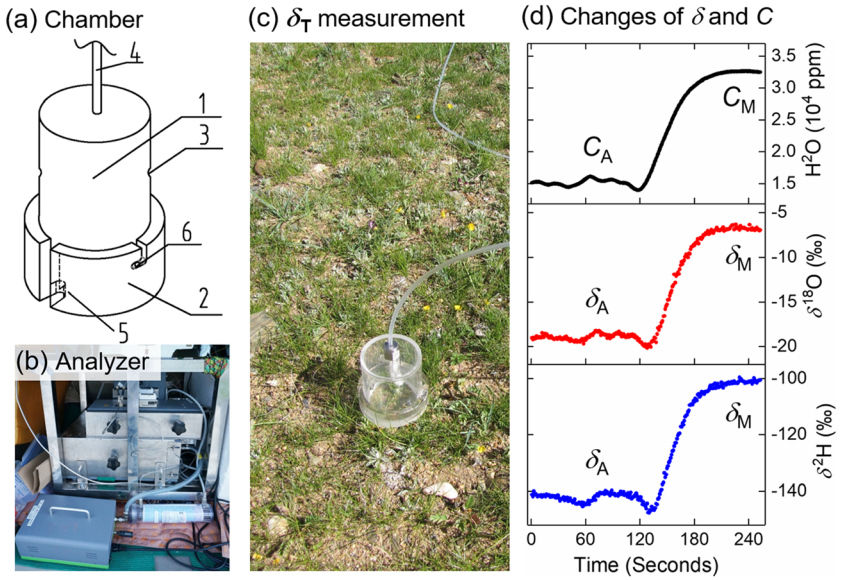

Figure 2. (a) Schematic of the leaf chamber structure. The chamber consists of two parts, a cap (1) and a base (2), made by transparent cylindrical acrylic. Plant samples are passed into the chamber through the small hole (5) on the base. Chamber then can be closed by rotating the cap and base and is fastened by two screws (6). Leaves transpired water vapor mixes with ambient water vapor entering through two air vents (3). Chamber air is sucked out through a Teflon tube (4) connecting the chamber to the water vapor isotope analyzer. For δ_E and δ_{ET}, the chambers just have a cap but with no base (not shown), the cap is directly placed on ground surface to measure δ_E or δ_{ET}. (b) Analyzer setup. Peripheral equipments include a standard delivery module and a vaporizer module and a vacuum pump. All the equipments were installed in a trolley for easy movement. (c) Photo of δ_T measurement (leaf chamber). (d) Changes of water vapor concentration (C) and isotope (δ) before and after chamber closure during a typical measurement. C_A and δ_A are the concentration and isotopic compositions of ambient water vapor before chamber closure, and C_M and δ_M are the concentration and isotopic composition of water vapor inside the chamber at the steady state after chamber closure.

level (Figure 2). The geology is Neotectonic development since the Quaternary with fault activity. The soil depth ranges from 0.5 to 2 m ("Lithic Leptosols" in the Food and Agriculture Organization soil classification). For soil texture, sand is a dominant component (>85%) from the surface to a depth of 40 cm, while clay content maintains a low value of less than 2%. Organic carbon content is 2.1% in topsoil (0- to 10-cm depth) and decreases with depth (Chen et al., 2012). The vegetation is alpine meadow, and the growing season occurs predominantly from June to September. According to our survey, plant species include *Kobresia pygmaea*, *K. humilis*, *Stipa purpurea*, *Potentilla bifurca*, and *Carex moorcroftii*. Among the five species at our site, *Kobresia pygmaea* dominates the vegetation coverage (80–90%), with an average canopy height of ~5 cm above ground level, while the below-ground biomass is mainly distributed at a depth of 0–10 cm. Our isotopic observations focused on *Kobresia pygmaea*.

2.2. Observation Systems

2.2.1. Isotope Measurements

A Picarro L2130-i wavelength-scanned cavity ring-down spectroscopy analyzer with high frequency (1 Hz) has been installed at the NPCE site since July 2014. The analyzer was placed in a room at the field site to ensure the stability of ambient air temperature. It can switch between two modes (i.e., solid mode and vapor mode) to measure the isotopic composition of plant and soil water samples (Cui, Tian, Gerlein-Safdi, & Qu, 2017), or land-surface water vapor, respectively (Steen-Larsen et al., 2013). The analyzer operated in tandem with other additional equipment, as follows. Plant stem (*Kobresia pygmaea*) and soil samples were measured by the analyzer in solid mode combined with an induction module CRDS 017 (IM, Picarro Inc., Santa Clara, CA). Three kinds of standard waters were used during the measurement: S1 ($\delta^{18}O = -6.94‰$), S3 ($\delta^{18}O = -18.33‰$), and S9 ($\delta^{18}O = -31.90‰$). S1 and S3 were used to calibrate measured isotope values to the Vienna Standard Mean Ocean Water (V-SMOW) scale, while S9 was employed regularly to evaluate the stability/drift of the analyzer. The solid mode allowed for the simultaneous measurement of the isotopic compositions of small solid samples and the removal of organic contamination from within the samples in

the field. For stems (defined as measured at the root crown, i.e., the nongreen position of the joining of root and stem below the soil surface), samples were collected by a shovel and were wrapped in small trifold metal strips (Picarro Inc., Santa Clara, CA) and placed inside a 4-ml glass vial. The vial was inserted into the IM and heated through induction. For the soil, samples were dug out with a hand drill, and at 5-, 10-, 20-, 30-, 50-, and 80-cm depths. Each sample (~4 μg) was put into a 20-mm-long and 5-mm-diameter steel tube (Picarro Inc., Santa Clara, CA) and also placed inside a vial to be measured. This process generally required 5 min to measure stem water and 10 min to measure soil water samples. About 3 μl of standard water (S1 and S3) was injected onto glass filter paper (Whatman plc, Maidstone, UK) to calibrate stem and soil samples to the V-SMOW reference. The precision for $\delta^{18}O$ was 0.35‰. The detailed measurement and calibration processes followed the protocol of Cui, Tian, Biggs, & Wen (2017). The depth with the most enriched soil water isotopes was set to be the evaporating front (Dubbert et al., 2013), and the corresponding isotopic values from that position were used to calculate δ_E.

In vapor mode, the measurement and calibration system comprised of a standard delivery module A0101, a vaporizer module A0211 (Picarro Inc., Santa Clara, CA), and an analyzer. During measurements, S3 and S9 (standard waters) were pumped from the standard delivery module to the vaporizer module (at 140 °C) to generate two kinds of standard water vapors. These were then mixed with dry air (Drierite filter, 8 mesh, W. A. Hammond Driterite Company, Ltd., USA), and then finally measured by the analyzer. Water vapor concentrations were regulated by a high-precision syringe (80 μl) pump. Each vapor concentration was measured for 20 min before the measurement of outside water vapor. Outside water vapor was then pumped to the analyzer through a 1/8″ inner diameter stainless steel tube; the flow rate of the analyzer was set at 200 ml/min. The warm temperature inside the room and the tube heated by the vaporizer prevented the condensation of water vapor in the flow path. Instrumental drifts and humidity dependence (Figure S1 in the supporting information) of water vapor isotopes were corrected before calibrating to V-SMOW reference following the protocols of Steen-Larsen et al. (2013) and Aemisegger et al. (2012). Water vapor isotopes were sampled at 0.1, 0.3, 0.5, 0.7, and 1.0 m above the ground, utilizing five-way solenoid valves and from 13:00 to 15:00 hr (local standard time, UTC + 6). Each level was sampled for 10 min, and the last 5 min was averaged to establish the Keeling plot. The precision was 0.2‰ for measured vapor $\delta^{18}O$.

In June–July 2016, the newer chamber method was used, and to directly measure the three end members, δ_T, δ_E, and δ_{ET} (Figure 2; Dubbert et al., 2014; Haverd et al., 2011; Lu et al., 2017; Volkmann et al., 2016; Wang et al., 2010). The sizes of the three chambers were 5 cm × 5 cm (diameter × height), 10 cm × 5 cm, and 20 cm × 5 cm, respectively. The setup of equipment was the same as that of vapor isotope measurement above, except that the vapor was instead pumped from the closed chamber. The analyzer and peripheral equipment were installed in a customized trolley (Figure 2b), which enabled us to take the chamber to different plots for easier measurement (Figure 2c). The field measurements were conducted typically during the no-rain periods (a full day or where a substantial part of a day is dry), and between 8:00 and 18:00 (local standard time, UTC + 6), and at an interval of 2 hr. In each cycle, the three end members were sequentially measured with three replicates at random locations. Each individual measurement usually required 4–5 min to complete, with precise timing dependent on the intensity of surface water fluxes. The daily T/ET were calculated as the sum of subdaily T/ET weighted by ET flux.

To evaluate the influence of the chamber size on the measured isotopic value, chambers with different sizes were used to measure one end member in the same plot. The aims were twofold. First, to test the representativeness of chamber coverage area. In particular, δ_{ET} was sensitive to the area fraction of vegetation or soil covered in the chamber, due to sparse vegetation coverage in this region (Figures 1c and 2c). For instance, δ_{ET} in small chamber would differ from that of big chamber (both soil and leaves fluxes) if vegetation in small chamber was not representative of local vegetation coverage. Second, to test for the presence of condensation inside the chamber or sampling line. The big chamber had a larger volume and therefore needed additional time to reach a steady state, and so confounding issues of condensation were more likely relative to small chamber in high-elevation ecosystems (low air temperature).

To validate the representativeness of δ_{ET} in chamber method, the independent Keeling plot approach was used for comparison as a benchmark. The Keeling plot was observed immediately after δ_{ET} chamber measurements were obtained at our observational sites. Water vapor isotopes were measured at two heights (0.5 and 1.5 m above ground) for 30 min. Each height was measured for 2 min, and the two heights were

switched every 2 min through a two-way solenoid valve. The last 0.5 min of each 2 min was used to establish Keeling plot. The comparison was conducted in the beginning (1 June 2016) and peak (15 July 2016) of the growing season. The observation was paused or ceased if rain or strong wind commenced, which would introduce foreign water vapor and thus bias measured results or disturb observations. The exactness of isotope-based results was demonstrated by good agreement between T/ET derived independently from $\delta^{18}O$ and $\delta^{2}H$. To evaluate the exactness of isotope-based T/ET in our study, we thus compared $\delta^{18}O$-derived and $\delta^{2}H$-derived T/ET based on chamber method. Precipitation samples for isotope analysis were also collected manually on every rainy day using an evaporation-preventing collector (Figure S2). The collector consists of a "V-shape" tube in the inlet to prevent water reevaporation and a 1-m-long internal tube for pressure equilibration, modified slightly from the design of Groning et al. (2012).

2.2.2. Meteorological and Eddy Covariance Observations

Air temperature and relative humidity were recorded using HMP155 sensors (Campbell Scientific Inc., Logan, UT, USA) at 2 m above the ground surface on a planetary boundary-layer tower. Precipitation was measured by a T-200B rain gauge (Geonor Inc., Augusta, NJ, USA). Wind speed and direction (020C-1, MetOne Inc., USA) were measured at a height of 10.36 m. Downward and upward long-wave and shortwave radiation (CNR4, Kipp & Zonen Inc., Netherlands) were measured at 2-m height. Soil temperature (AV-10 T, Avalon, Jersey City, NJ, USA) and θ (ECH_2O, Decagon, Pullman, Washington, USA) were recorded at 0.04- and 0.2-m depths. The observations of θ were under the guidance of standard soil moisture measurements (Yang et al., 2013). The bias in θ measurements introduced by organic carbon content (2.1% in topsoil at our observational site) is small (less than 5.7%; Yang et al., 2013). The θ measured at NPCE site has been widely used in model validation (Xue et al., 2013) and the evaluation of satellite soil moisture (Ma & Ma, 2019). All meteorological data were recorded at 30-min intervals. Eddy covariance (EC) instruments, consisting of an open path infrared CO_2/H_2O gas analyzer (LI-7550, LI-COR Inc., USA) and a three-dimensional sonic anemometer thermometer (CSAT3, Campbell Scientific Inc., USA), were installed at a height of 3 m above the ground to measure ET.

LAI was measured using a direct harvesting method (Bréda, 2003), with a time interval of approximately 1 week during June–July 2016. In the LAI measurement, all the leaves above ground and within a 0.5 m × 0.5 m square were harvested, and the areas of all the collected leaves were determined by scanning. To test whether measured LAI had reached it maximum of the year, and at the end of our observations in 2016, we analyzed 500-m resolution and 8-day composite Moderate Resolution Imaging Spectroradiometer (MODIS) LAI for the months afterward. This data set (MOD15A2H) gave the full year of LAI (data from https://lpdaac.usgs.gov/products/mod15a2hv006). The seasonal cycle of MODIS LAI was extracted for the location of our observational site. The values proved to be broadly consistent with observations (Yan et al., 2016).

2.3. *ET* Partitioning Approaches

2.3.1. Isotope-Based Method

Water stable isotopes have been widely used to estimate plot-scale ET partitioning (Good et al., 2014; Wang et al., 2010; Wei et al., 2015; Williams et al., 2004; Yepez et al., 2003). This approach is possible because isotopic fractionations result in distinct isotopic signals of δ_{ET}, δ_E, and δ_T. Based on isotopes and water mass balance, these allow calculation of the T/ET ratio, satisfying the equation (Yakir & Sternberg, 2000):

$$\frac{T}{ET} = \frac{\delta_{ET} - \delta_E}{\delta_T - \delta_E} \tag{1}$$

where δ_{ET}, δ_E, and δ_T are isotopic compositions of ET, soil evaporation (E), and plant transpiration (T), respectively. $\delta = R_{sample}/R_{standard} - 1$, and the value of the isotopic composition (δ) is expressed per mil (‰) relative to the V-SMOW scale. R is the isotopic ratio $^{18}O/^{16}O$ or $^{2}H/^{1}H$. For the experiment performed in June–July 2016, the chamber-based isotope measurement was used to determine the three isotopic end members directly (chamber method). However, in 2014, we instead used the Keeling plot and CG model (Keeling-CG method) to estimate isotopic compositions, allowing us to implement the two theories separately.

2.3.1.1. Chamber-Based Method

Recently, the chamber method was introduced to directly measure the isotopic composition of δ_T (Dubbert et al., 2014; Wang et al., 2010), δ_E (Dubbert et al., 2013), or all three end members (Lu et al., 2017; Wang et al.,

2013). For the chamber method in our study, three kinds of transparent cylindrical acrylic chambers were developed to measure δ_T, δ_{ET}, and δ_E of the alpine meadow ecosystem, following Wang et al. (2012; Figures 2a and 2c). For δ_T, the chamber consists of two parts, a cap and a base. Plant leaves were first placed into the chamber through the inlet on the base. The chamber was then sealed by rotating the cap and base, joined at a neoprene gasket, and the two parts were tightly fastened by two screws (Figure 2a). Two small air vents on the cap were the only path that allowed for ambient air to enter the chamber and mix with vapor transpired by the leaves. The mixed vapor was finally pumped to the analyzer through a 3-m-long and 1/8″ inner diameter tube (consisting of a 0.5-m Teflon tube and a 2.5-m stainless steel tube; Figure 2b) for isotopic analysis. The residence time of vapor in the tube (total volume: 23.7 cm^3) is only 8 s at a flow rate of 200 cm^3/min, which is negligible in terms of the chamber measurement. Furthermore, to avoid the influence of residual vapor from previous measurements in the tube on the isotopic compositions, an interval (~2–3 min) was left between them. Hence, the next measurement should occur after vapor concentration and isotopic composition in the analyzer have dropped back to background levels. For the measurement of δ_{ET} and δ_E, only the cap was used. The cap was directly placed on areas with both soil and plants to measure δ_{ET}, and on bare soil only (i.e., in the gaps between vegetation), to measure δ_E. The cap was tightly covered on the ground to seal the chamber. This procedure ensured that ET (δ_{ET}), or only soil evaporation vapor (δ_E), as mixed with ambient air from air vents on the cap, was measured by the analyzer. In the course of measurement, we first measured ambient vapor for 2 min and then closed the chamber and measured mixed water vapor for another 2 min (Figure 2d). The concentration and isotopic composition of water vapor in the chamber reached a steady state (showed little change with time) after ~1–1.5 min. The concentrations and isotopic compositions of water vapor for the first 2 min and then the last 0.5 min (30 data points) were averaged individually. This provided, respectively, ambient and steady-state values to calculate the three end members. Based on isotope and water mass balance, the isotopic composition of source water vapor, δ (δ_T, δ_{ET} or δ_E), was calculated as (Wang et al., 2012)

$$\delta = \frac{C_M\delta_M - C_A\delta_A}{C_M - C_A} \tag{2}$$

where C_A and δ_A are the concentration and isotopic compositions of ambient water vapor and C_M and δ_M are the concentration and isotopic composition of mixed water vapor in the chamber at the steady state.

A previous study has shown that there is a strong humidity dependence of the vapor isotope for laser-based isotopic analyzer (Gupta et al., 2009). Due to the large change of vapor concentration before and after chamber closure (Figure 2d), all water vapor isotopes were calibrated to a reference humidity level (20,000 ppm) based on the established humidity-isotope relationship (Figure S1), in order to remove the impacts of vapor concentration change. Including a source of dry air within the chamber to replenish the air pumped by the analyzer may increase the net water vapor availability within the chamber (e.g., Wang et al., 2010). Although no source of dry air was added in our experiment, the transpired or evaporated water vapor inside the chamber was at a much higher level (Figure 2d), satisfying the necessary water vapor for the chamber method. This approach (without a source of dry air) has been successfully applied in diverse ecosystems (Dubbert et al., 2014; Good et al., 2014; Lu et al., 2017; Wang et al., 2013).

2.3.1.2. Keeling-CG Method

For the Keeling-CG method, the Keeling plot was used to determine δ_{ET} (Good et al., 2014; Keeling, 1958; Wei et al., 2015; Yakir & Sternberg, 2000; Yepez et al., 2003). The measured water vapor was a mixture of background water vapor and *ET* released from the ecosystem. Based on the linear regression between measured water vapor isotope (δ_V) and the reciprocal vapor concentration value at multiple heights over a specific time interval, δ_{ET} was calculated as

$$\delta_V = C_B(\delta_B - \delta_{ET})\left(\frac{1}{C_V}\right) + \delta_{ET} \tag{3}$$

The intercept is equal to δ_{ET}, where C_V and C_B represent the concentrations of measured water vapor and background water vapor, and δ_B is the isotopic composition of background water vapor. It is assumed that δ_{ET} and δ_B remain constant over the course of observations.

Taking into account both equilibrium and kinetic fractionation during the phased change of water from liquid to vapor, the CG model (Craig & Gordon, 1965) was widely employed to determine δ_E and has been successfully applied in different conditions (Good et al., 2014; Rothfuss et al., 2010; Wei et al., 2015; Yepez et al., 2003). We calculated δ_E using the following equation (Craig & Gordon, 1965; Good et al., 2014; Horita et al., 2008; Wang et al., 2010):

$$\delta_E = \frac{\alpha^* \delta_S - h\delta_V - (\varepsilon^* + \varepsilon_K)}{1 - h + 10^{-3}\varepsilon_K} \tag{4}$$

where the vapor-liquid equilibrium fractionation factor α^* (<1) is calculated as a function of temperature at the evaporating front (T_S), following Horita and Wesolowski (1994). Here $\varepsilon^* = (1 - \alpha^*) \times 1{,}000$ is the equilibrium enrichment factor; δ_V is the isotopic composition of ambient water vapor and δ_S is the isotopic composition of soil water at the evaporating front; and h is the relative humidity normalized to the saturated vapor pressure at T_S. The kinetic enrichment factor, ε_K, is defined as

$$\varepsilon_K = n(1 - h)\left(\frac{D}{D_i} - 1\right) \times 10^3 \tag{5}$$

where D/D_i is the molecular diffusion coefficient of the vapor isotope. Though different values have been estimated (Cappa et al., 2003; Merlivat, 1978), the commonly used value for oxygen, 1.0285, was used in this study (Good et al., 2014; Rothfuss et al., 2015; Yepez et al., 2003). The aerodynamic diffusion parameter n is related to the volumetric soil water content (denoted by θ), as proposed by Mathieu and Bariac (1996), and varies from 0.5 for saturated soil conditions to 1.0 for dry soil. Thus:

$$n = \frac{(\theta_o - \theta_r)n_a + (\theta_s - \theta_o)n_s}{\theta_s - \theta_r} \tag{6}$$

where $n_a = 0.5$ and $n_s = 1$, and subscripts o, s, and r refer to soil surface, saturated, and residual θ values, respectively. Residual and saturated θ were represented by minimum (0.01 m^3/m^3) and maximum (0.34 m^3/m^3) values throughout the observation (Dubbert et al., 2013). At midday and in the early afternoon when ET was most intense, we assumed that δ_T was equal to the isotopic composition of plant water source under isotopic steady state (ISS; Wei et al., 2015; Wen et al., 2016; Xiao et al., 2012; Yakir & Sternberg, 2000).

2.3.2. Two-Source Model Method

To independently compare to our isotope-based T/ET results, a two-source model was used to partition ET, following Wang and Yamanaka (2014). This method has been successfully applied in different ecosystems (Wang, Li, et al., 2016; Wang et al., 2018). Based on the radiation/energy balance at both the vegetation canopy and the ground surface, the model partitioned ET into canopy transpiration and soil evaporation at the hourly timescale (Appendix A, (A1)–(A3)). This model therefore isolated and estimated evaporation from soil surface (E) and transpiration from the canopy (T) as two separate sources (Appendix A, (A4)–(A5)). Four resistance parameters, that is, aerodynamic resistances for vegetation canopy and for the ground surface, canopy (stomatal) resistance and surface soil resistance, were used to model the transport of water fluxes from canopy or soil surface to the atmosphere. Detailed descriptions and parameterizations of the two-source model are presented in Appendix A. Required meteorological and ecological input data are air temperature, relative humidity, wind speed, downward longwave and shortwave radiation, albedo, soil temperature and water content, LAI, and canopy height. To test the performance of two-source model, the simulated results were compared against the EC observations.

2.4. Sensitivity Analysis

A sensitivity analysis was conducted for both chamber and Keeling-CG methods to attribute the uncertainties and possible error sources from each input parameter (or variable) of equations (1) and (4). The sensitivity was quantified using Crystal Ball software (Oracle Inc., Redwood City, CA), which implements a Monte Carlo simulation. In the simulation, 10,000 trials were created by subsampling input parameters and determining their influence on T/ET estimates, represented by their measured standard deviations in an assumed normal distribution. However, the bias may be induced if input parameters were not normally distributed (e.g., an average error of 5 percentage points of estimated sensitivity for a skewed distribution relative to a

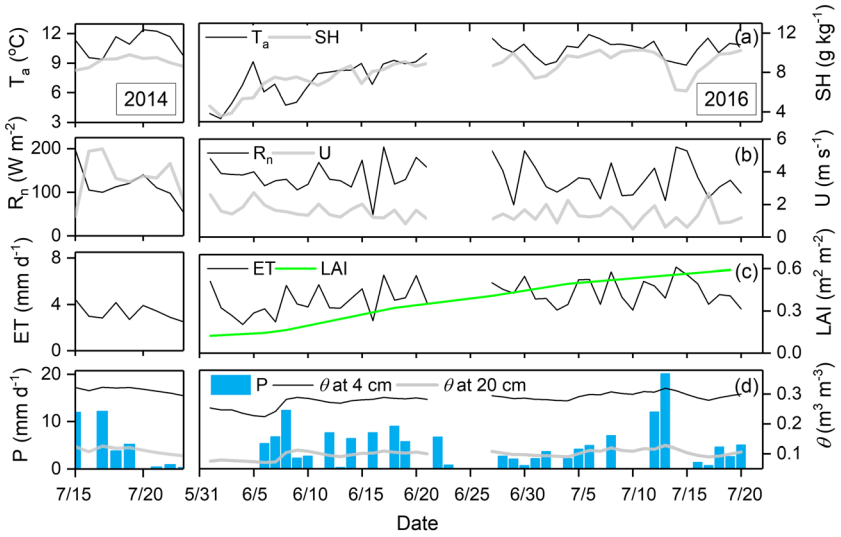

Figure 3. Seasonal variations of daily air temperature (T_a) and specific humidity (SH) at 2 m above ground, wind speed (U) at 10.4 m above ground, net radiation (R_n), daily eddy covariance-derived evapotranspiration (ET), leaf area index (LAI), daily precipitation (P), and soil water content (θ) at 4- (black line) and 20-cm depth (gray line) during the two periods of observations. Meteorological data were unavailable from 22 to 26 June 2016 due to electricity outage.

normal distribution of input parameters). Specifically, the sensitivity here was defined as the percentage change in T/ET induced by a change of each input parameter. For Keeling-CG method, we further calculated the sensitivity of δ_E to each input parameter in CG model (Craig & Gordon, 1965; Horita et al., 2008). The advantage of Monte Carlo-based Crystal Ball software is that it could quantify the contribution percentage of each input parameter to the change of T/ET in the case of all input parameters changing at the same time (Cui, Tian, Biggs, & Wen, 2017).

For the three isotopic end members, δ_T, δ_{ET}, and δ_E, the uncertainty was calculated based on the measured standard deviation of each input parameter, then propagated through equations (2), (3), or (4) for each individual measurement (Good et al., 2014; Wei et al., 2015). Based on field observations, the uncertainties of end members δ_{ET}, δ_T, and δ_E in the chamber method for $\delta^{18}O$ (δ^2H) were 0.7‰ (4.2‰), 1.1‰ (4.6‰), and 0.8‰ (4.7‰), respectively, while the uncertainties of δ_{ET} (Keeling plot) and δ_E (CG model) in Keeling-CG method for $\delta^{18}O$ were 1.1‰ and 1.0‰. For the two-source model, sensitivity analysis indicated that modeled T/ET was more sensitive to the change in LAI (Wang & Yamanaka, 2014).

3. Results

3.1. Seasonal Variations in Meteorological and Biotic Variables

Figure 3 shows the variations of daily meteorological variables and LAI during the observation periods in years 2014 (left column) and 2016 (right column). Mean daily air temperature was 9.7 °C during the two periods of observation, and air temperature variations broadly regressed ($y = 0.63x + 2.5$, $R^2 = 0.64$) with fluctuations in specific humidity (Figure 3a). Average wind speed was 1.5 m/s in 2016, whereas in 2014 there was relatively higher mean wind speed of 3.6 m/s, varying from 1.2 to 5.3 m/s (Figure 3b). LAI increased from about 0.1 m^2/m^2 at the beginning of June to 0.6 m^2/m^2 at the end of observations in 2016 (Figure 3c). This was lower than the peak LAI of ~1 m^2/m^2 at the nearby Damxung station (Hu et al., 2009). Satellite-based estimates of LAI indicated that LAI reached a growing-season maximum in this area around 20 July, which is at the end of our observations in 2016 (data not shown). EC measured ET, ranged from 2.5 to 7.4 mm/day, with an average of 4.7 mm/day. Daily mean precipitation was 3.2 mm/day during observation periods, and θ at 4- and 20-cm depths showed similar variations in response to precipitation events (Figure 3d).

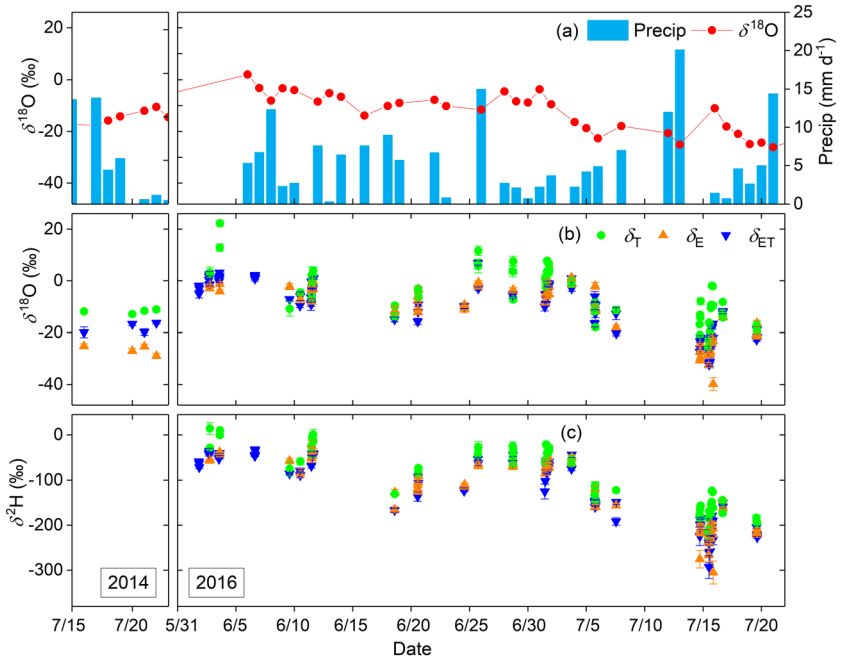

Figure 4. Seasonal variations of (a) precipitation amount and precipitation $\delta^{18}O$, δ_T (green circles), δ_E (brown triangles), and δ_{ET} (inverted blue triangles) for panels (b) $\delta^{18}O$ and (c) $\delta^{2}H$. Shown in all rows are for the two periods of observations (as marked). The multiple points on a given day is measurements at a 2-hr interval during each day. The error bars depict the standard deviation for δ_T, δ_{ET}, and δ_E in each measurement. The experiment was unavailable from 12 June to 16 June, from 21 June to 23 June, and from 8 July to 12 July due to the loss of electric power.

3.2. Seasonal Variations of δ_T, δ_{ET}, and δ_E

Figure 4 illustrates the temporal variations of the three isotopic end members, along with precipitation $\delta^{18}O$ and precipitation amount. In 2016, δ_T, δ_{ET}, and δ_E showed large temporal variations, with a range of −39.9 to 22.2‰ for $\delta^{18}O$ and −305.1 to 14.1‰ for $\delta^{2}H$. At the beginning of June, the three end members were more enriched in heavier isotopes, with an average of 0‰ for $\delta^{18}O$ and −50‰ for $\delta^{2}H$. Then they decreased before reaching a plateau at the end of June. The minimums were achieved in the middle of July, as along with a sharp decrease of precipitation $\delta^{18}O$. The consistent variations of the three end members and precipitation $\delta^{18}O$ ($R^2 = 0.53$, $p < 0.001$) suggest that the former was strongly affected by precipitation isotopes. The short-term observations in June 2014 showed depleted $\delta^{18}O$ in the three end members, which agreed with the lower $\delta^{18}O$ in July of 2016. The temporal variations of $\delta^{18}O$ in the three end members and precipitation during our observation periods were consistent with the typical seasonality of precipitation isotope of maximum value known to occur in spring and earlier summer, and with a minimum in the mature summer on the TP (Tian et al., 2007; Yao et al., 2013). These values imply that our observational periods span from spring to summer seasons and are representative of the typical seasonal precipitation isotope characteristics.

In general, δ_T was the most enriched end member, followed by δ_{ET} and then by δ_E (Figure 4). This sequence of magnitudes was because ET was a mixed water vapor from both soil evaporation and plant transpiration. However, of note, this order was not met in some days, for example, $\delta_E > \delta_{ET}$ in early June and July. Two factors may account for this phenomenon. First soil water isotopes in this area were spatially heterogeneous, and thus, δ_E was enriched in some plots. Second,, when transpiration was intensive in the noon, water vapor might condensate in the wall of the chamber due to the low air temperature (high elevation), lowering δ_T and δ_{ET} but within the precision of chamber method (Wang et al., 2012). The three end members were filtered following the quality control of Wang et al. (2013; excluding data with instrumental malfunctions and obvious errors, e.g., $\delta_E > \delta_{ET}$), and the resultant data ($\delta_T > \delta_{ET} > \delta_E$) then used in the calculations of the next section.

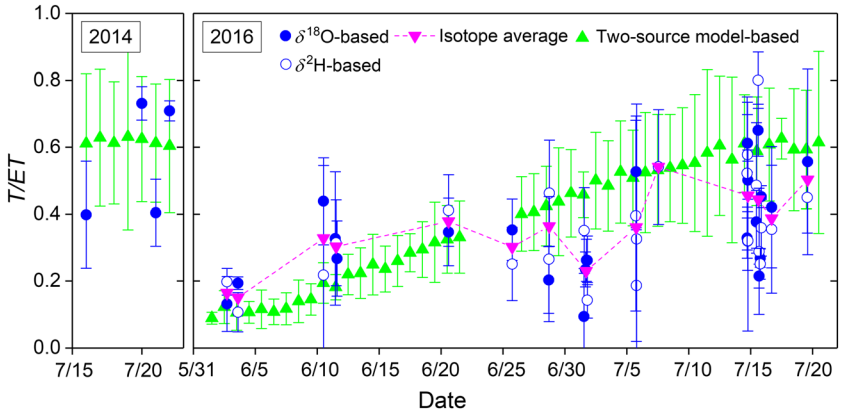

Figure 5. Temporal variations of δ^{18}O-based (solid blue circles) and δ^{2}H-based T/ET (open blue circles) and their daily average (inverted pink triangles) during the two periods of observations. Daily T/ET derived from the two-source model and eddy covariance was also presented as a comparison (green triangles). The error bars depict the standard deviation for δ_T, δ_{ET}, and δ_E in each measurement.

3.3. Seasonal *ET* Partitioning and its Controls

Using the observed values of δ_T, δ_{ET}, and δ_E, we derived the daily value of T/ET (Figure 5) based on equation (1). In 2016, isotope-based T/ET broadly increased, although with fluctuations during the observational periods. Specifically, T/ET was in the range of 0.1–0.2 at the beginning of June, then rose to nearly 0.4 in mid-June, before slightly decreasing during the end of June, and then finally increasing to 0.5 at mid-July. Isotope-based T/ET during the short-term observation in year 2014 also showed large variations. T/ET on 16 and 21 July was 0.4, whereas it was as high as 0.7 on 20 and 22 July. For two-source model-based T/ET, it increased nearly linear with time in 2016 and reached a maximum value of 0.6 at the end of observations. In 2014, however, modeled T/ET seemed in a horizontal line due to the short period of observations (1 week). On average, isotope-based T/ET was 0.43 during the two periods of observations, although recognizing substantial temporal variations. This mean result was supported by the T/ET value (0.48) as derived from EC measurements combined with two-source modeling (Wang & Yamanaka, 2014; Figure 5 and Appendix A). Although the average modeled T/ET was consistent with that of isotope-based results (0.48 vs 0.43) during the periods of observation, the seasonal variations of T/ET between them were different (Figure 5), indicating some deficiencies in the parameterization of the two-source model. Based on isotope-based T/ET values, EC flux data were further partitioned into T and E (Figure 6). In days with no isotope observation, T/ET was linearly interpolated between its recorded values at adjacent days, as a first-order approximation. This was reasonable because meteorological conditions generally did not show large fluctuations during several adjacent days (Figure 3). While T/ET values calculated from the two-source model changed smoothly during observational periods (Figure 5). Overall, T increased with the increase of LAI, with an average rate of 0.5 mm/day at the beginning of June, rising to substantially larger values greater than 2 mm/day at the end of our observations. However, E varied by a much smaller amount during the measurement period in 2016. This confirmed that the increase of ET was in association with enhancement of plant activity.

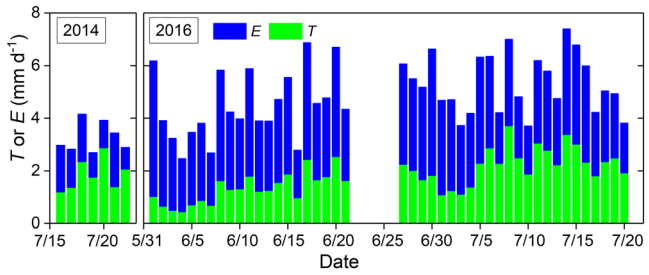

Figure 6. Seasonal variations of daily T (green columns) and E (blue columns) calculated from isotope-based T/ET and eddy covariance measured ET. In days with no isotope observation, T/ET was linearly interpolated by T/ET at adjacent days as a first-order approximation.

In addition to LAI, we found evidence that T/ET variations were also controlled by θ. There was evidence that θ at 4-cm depth played a critical role in the changes of T/ET (Figure 7b). T/ET increased with elevated θ, suggesting that θ was another potential driver of T/ET change. To calculate the contribution of individual driver to T/ET change and to remove any compounding effects, we further performed a partial correlation analysis between T/ET and a set of different forcings. The partial correlation coefficients between T/ET and θ, LAI, vapor pressure deficit, and T_a were 0.62, 0.22, 0.07, and 0.01, respectively (Figure 7c).

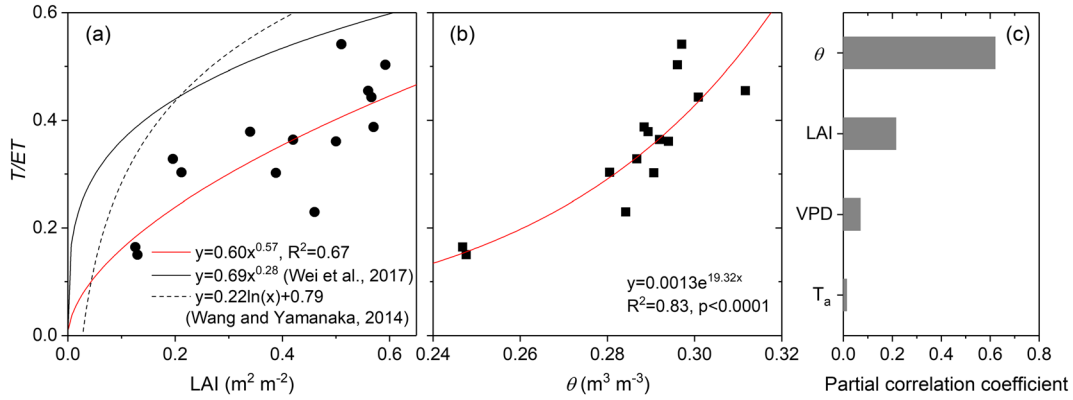

Figure 7. Relationships between daily isotope-based T/ET and (a) leaf area index (LAI) and (b) θ at 4-cm depth and (c) partial correlation coefficients between T/ET and θ, LAI, vapor pressure deficit (VPD) and T_a at Nagqu Station of Plateau Climate and Environment station. Data from 2014 were not included due to the absence of LAI observations. Regressions for shrubs and grasses from a global observation data set (Wei et al., 2017; black solid line) and for a temperate grassland (Wang & Yamanaka, 2014) (dash line) were also presented (a).

4. Discussion

4.1. Performance of Chamber Method on the TP

The advantage of using the chamber method to partition ET was its sequentially direct measurement of the necessary three isotopic end members (Dubbert et al., 2014; Wang et al., 2010). Such direct measurements bypassed the need to utilize isotopic models, along with their complex (and sometimes uncertain) parameterizations. The performance of chamber method has already been evaluated in different ecosystems. For example, Wang et al. (2012) found that the precision of the δ_T chamber was 1.0‰ and 1.6% for $\delta^{18}O$ and δ^2H, respectively, using water vapor with known isotopic composition in laboratory experiments. It was later suggested that the results of the chamber method were consistent with those of the Keeling plot approach for different isotopic end members, based on a controlled experiment in a farmland field (Wang et al., 2013). Dubbert et al. (2013) found that chamber-based δ_E was in good agreement with the Craig and Gordon model in an open cork-oak woodland. However, until our analyses, the overall performance in high-elevation grassland remained unknown. Here for the first time, we evaluated use of the chamber method in an alpine meadow in the central TP. We have paid particular attention to the risk of biases in using the chamber method, should condensation occur inside the chamber. Condensation is a particular issue for low air temperatures in high-elevation ecosystems.

As three chambers with different sizes were used in this study to measure δ_T, δ_{ET}, and δ_E, respectively, we first checked whether there was any influence of chamber size on measured isotopic values. Figure 8 shows the results of the three isotopic end members from three different sizes of chambers. All of δ_T, δ_{ET}, and δ_E were consistent between results of the two chambers for both $\delta^{18}O$ and δ^2H, with a high R^2 of 0.93 and 0.97, and an average difference of 0.6‰ and 0.5‰, respectively. These statistics are encouraging and imply that the influence of chamber size on isotopic values was negligible. Furthermore, the consistent results between small and big chambers for δ_{ET} suggested that vegetation in the δ_{ET} chamber was representative of local vegetation coverage. In addition, no significant signal of condensation was observed despite longer times to reach steady state for big chamber. However, when δ_E was extremely small (see data in the lower left corner of Figure 8a), $\delta^{18}O$ of δ_E from the small chamber (−29.7‰) was significantly different from that of big chamber (−24.5‰). One possible reason accounting for this large difference was the heterogeneity of the soil water isotope. This may have resulted in different δ_E estimates in the soil evaporative vapor, due to variations in soil surface coverage caused by the different diameters of the two chambers. In addition, the two chambers were used in measurements sequentially, with an interval of 10 min, and δ_E may change with time.

We then evaluated the uncertainty and accuracy of the chamber method. The average standard deviation of $\delta^{18}O$ and δ^2H were 0.7‰ and 4.5‰ during the observations of 2016. While the standard deviation of $\delta^{18}O$ is very close to the precision of laboratory-based values, of 1.0‰ of Wang et al. (2012), the standard deviation of

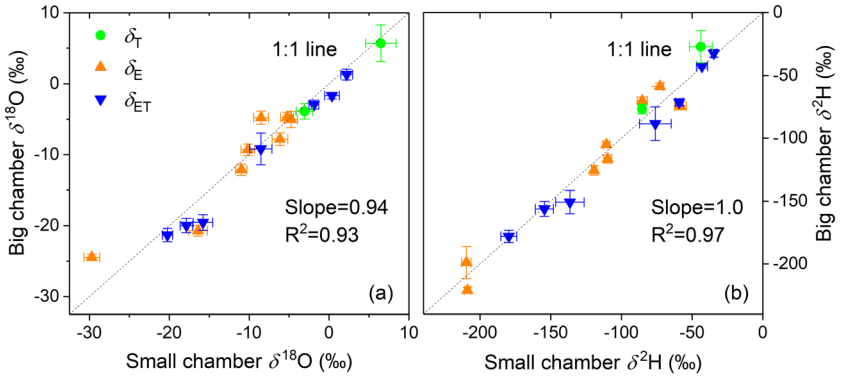

Figure 8. Comparisons of δ_T (green circles), δ_E (brown triangles), and δ_{ET} (inverted blue triangles) measured by two different sizes of chambers respectively for (a) $\delta^{18}O$ and (b) δ^2H. The sizes of small (big) chambers for δ_T, δ_E, and δ_{ET} are 5 cm × 5 cm (10 cm × 5 cm, diameter × height), 5 cm × 5 cm (10 cm × 5 cm), and 10 cm × 5 cm (20 cm × 5 cm), respectively. The error bars depict the standard deviation for δ_T, δ_{ET}, and δ_E in each measurement.

δ^2H is higher that of Wang et al. (2012; 1.6‰). The larger standard deviation for δ^2H may be due to its longer time to reach a steady state than that of $\delta^{18}O$, fluctuations of ambient conditions (C_A and δ_A; Figure 2d), possible occurrence of air condensation inside the chamber or sampling line. The impact of data processing on the standard deviation for δ^2H is small. Although the standard deviation of δ^2H was 4.5‰, its relative error was much lower, because the vapor isotope on the TP can as low as −300‰ due to the high elevation (Figure 4). There was no significant difference of standard deviation between δ_T, δ_{ET}, and δ_E.

Our results also show that $\delta^{18}O$-derived T/ET was consistent with the δ^2H -derived results (Figure 9), with values generally close to the 1:1 line. The values have a standard deviation of 0.08 and 0.13, respectively, indicating that $\delta^{18}O$ has a higher precision than δ^2H in T/ET estimation. An overall summary statistics is that the averaged relative difference of $\delta^{18}O$- and δ^2H-based T/ET values was 0.11. The difference may be related to uncertainties of the three isotopic end members or possible occurrence of water vapor condensation inside the chamber or sampling line. Hence, the accuracy of chamber method in T/ET estimation was about 0.11 on the TP, close to that of previous studies (Berkelhammer et al., 2016; Wei et al., 2018; Wu et al., 2016).

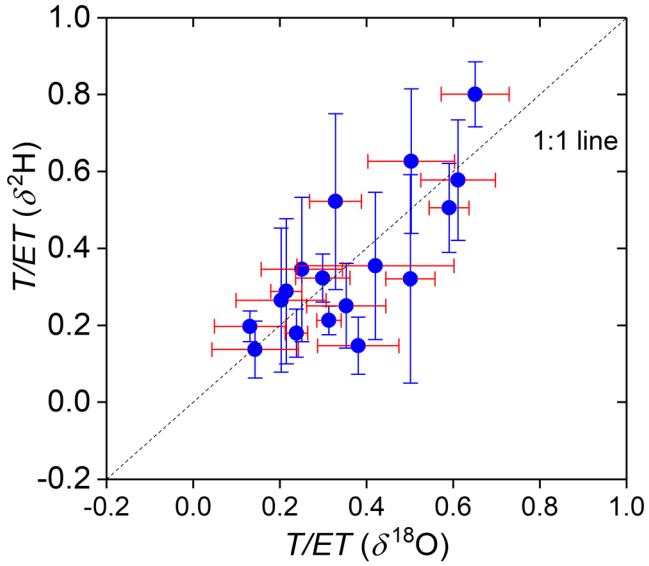

Figure 9. Comparison of $\delta^{18}O$- and δ^2H -based T/ET. The red and blue error bars depict the standard deviation for $\delta^{18}O$- and δ^2H -based results derived from the uncertainties of δ_T, δ_E, and δ_{ET} measurement.

We note that the agreement between the two-source model simulated ET and EC-observed ET ($R^2 = 0.81$) does not automatically assure that the partitioning between T and E in the two-source model is accurate. In the future, independent observational methods should be employed to further evaluate the chamber method, such as Keeling plot approach (Wang et al., 2013), lysimeter, and EC methods (Sutanto et al., 2014; Wei et al., 2018; Wen et al., 2016; Wu et al., 2016), as well as methods to isolate further the individual T and E components.

4.2. Underlying Mechanisms of T/ET Variations on the TP

Previous studies have consistently demonstrated that there is an observable relationship between T/ET and LAI at the seasonal scale (Berkelhammer et al., 2016; Hu et al., 2009; Wang et al., 2014; Wang et al., 2018; Wang & Yamanaka, 2014; Wei et al., 2015; Wu et al., 2016). Our isotope-based results reconfirmed this relationship, verifying that LAI plays an important role in the hydrological cycle of alpine meadow ecosystems, even though in areas the maximum LAI was relatively low, at less than 1 m^2/m^2. Recently, Wei et al. (2017) synthesized global published studies and found T/ET increased very quickly with rising LAI in shrub and grassland ecosystems, even under low LAI conditions (black solid line in Figure 7a). However, in our studied alpine meadow grassland ecosystem, the fitted function (red line) predicted T/ET considerably

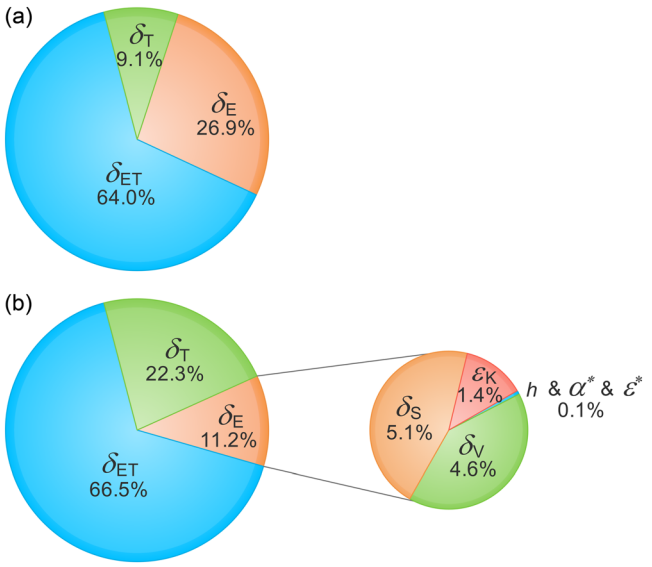

Figure 10. Percentage contributions (sensitivity analysis) of input parameters to the variations of T/ET in (a) chamber method and (b) Keeling-CG method. In (b), we further calculated the sensitivity of δ_E to input parameters in Craig-Gordon model (Craig & Gordon, 1965). δ_S and δ_V are the isotopic compositions of soil water at the evaporating front and of ambient water vapor. ε^* and ε_K are equilibrium and kinetic enrichment factor, respectively. α^* is equilibrium fractionation factor and h is relative humidity. The sector labeled 64.0% and δ_{ET} in (a) indicates that 64.0% of variations of T/ET is induced by the change in δ_{ET}, and so forth.

below that of Wei et al. (2017). This lower value may be due to the limitation of water availability, especially for low LAI values in spring when precipitation was small. Similarly, the function (dashed line, Figure 7a) from a temperate grassland of Wang and Yamanaka (2014) was close to that of Wei et al. (2017). However, annual mean precipitation (1,159 mm) in the former study was 2.5 times that at the NPCE site in our study. Furthermore, as agricultural plants are typically less limited by environmental stress, the T/ET-LAI relationship for our natural grassland ecosystem can be expected to be below that of agriculture (Wang et al., 2014). These factors suggest the important role of water availability in regulating the relationship of T/ET and LAI. Critically, we found the influence of θ to be of sufficient magnitude that it was comparable to the impact of LAI on T/ET (Figures 7a and 7b). Furthermore, partial correlation analysis even suggested that the individual contribution from θ was more substantial than that of LAI (Figure 7c). Hence, both physical (partial correlation coefficient: 0.62) and biological factors (0.22) dominated the variations of T/ET in our alpine meadow zone in central TP, which is different from previous studies that argue that T/ET was mainly controlled by LAI (Hu et al., 2009; Wang et al., 2014; Wang & Yamanaka, 2014; Wei et al., 2015)

Based on the observations at the NPCE site, we have developed an explanation of the underlying mechanisms controlling the changes of T/ET at seasonal scales. The lower T/ET in spring was related to the lower LAI in the early stage of the growing season, combined with lower θ corresponding to less precipitation. LAI reached a peak in summer, and intense precipitation elevated θ, and thus brought sufficient water for high levels of plant transpiration. Although T/ET was well correlated with θ at the NPCE site (Figure 7b), the relationship may have regional variation and not be ubiquitous, instead being climate type-related or soil type-related. For example, a global T/ET data set, as synthesized by Wang et al. (2014), showed generally low correlations with soil water potential. However, θ was a constraining factor in arid or semiarid climates (such as the TP), but less so in humid or semihumid climates. Limited studies that have reported this θ dependence to date were located in croplands (e.g., Liu et al., 2002 ; Wei et al., 2018). Yet croplands were often irrigated to improve crop yield and therefore less constrained by water availability, thus limiting the dependence of variations of T/ET on θ. Indeed, this may explain the opposite T/ET-θ relationship between previous studies (Liu et al., 2002; Wei et al., 2018) and our study. In addition, in ecosystems dominated by deep-rooted vegetation, these plants can take up water from deep soil or even groundwater when the surface soil was very dry (Maxwell & Condon, 2016), again causing weak correlations between T/ET and θ.

One caveat is that our two periods of field experiments were for the spring and summer periods only and therefore did not cover a full growing season. A longer timeframe might demonstrate T/ET to have slightly different LAI and θ dependencies at the NPCE site. Future measurement campaigns that cover a full growing season will enable testing of our discovered relationships between T/ET, LAI, and θ during other seasons.

4.3. Uncertainty and Possible Error Source in T/ET Ratio Estimation

Two independent isotopic methods were used for our observations. In year 2016, the chamber method was used, while in 2014, the Keeling-CG method was used. Here we discuss their respective sensitivity analysis and possible error source. Figure 10 shows the percentage contributions (sensitivity analysis) of each input parameter to the change of T/ET. For the chamber method, δ_{ET} dominated two thirds of the variations of T/ET, following by δ_E and δ_T (Figure 10a). Hence, an accurate determination of δ_{ET} was a particular priority. Although chambers with different sizes showed consistent δ_{ET} results (Figure 8), the use of chamber method may still be subject to biases in the measurement of δ_{ET} due to the small chamber size used (20 cm in diameter). We compared the δ_{ET} results between the chamber and conventionally-used Keeling plot approaches and found that they were generally consistent for $\delta^{18}O$ (chamber minus Keeling plot, −0.2‰ on average). However, for δ^2H, this was underestimated (−21.5‰ on average) by the chamber method

(Figure S3). Although the isotopic difference was much larger for δ^2H, its relative impact was low (~10%), because the value of δ_{ET} on the TP can be as low as −200‰. Overall, these differences indicated that vegetation in the δ_{ET} chamber is representative of local vegetation fraction, although we also suggest that more extensive comparison is necessary due to the current limited observations utilized in both methods in this study. The use of a larger chamber (e.g., 50 cm × 50 cm × 50 cm; Wang et al., 2013) may also be preferable in future study to reduce the bias of vegetation or soil fraction in δ_{ET} chamber.

An inherent limitation of the chamber method was its impact on environmental conditions inside the chamber, potentially affecting the measured isotopic values (Dubbert et al., 2014; Wang et al., 2012). For example, Dubbert et al. (2014) observed that air temperature in the chamber increased ~2 °C above ambient levels after 5 min in an open cork-oak woodland. This warming inadvertently enhanced estimated soil evaporation in the chamber, enriched δ_E relative to the CG model (Wang et al., 2013), and thus underestimated T/ET (Wu et al., 2016). Reducing the duration of chamber closure would diminish the impact of the chamber. Hence, we used only 2 min in this study, which is relatively short compared to previous studies, such as up to 10 min (Dubbert et al., 2013; Dubbert et al., 2014), 5 min (Wang et al., 2012), and 3 min (Good et al., 2014), although we match 1–2 min (Lu et al., 2017). Air temperature inside our chamber would have increased by only 0.8 °C after 2 min, assuming the same warming rate as Dubbert et al. (2014), although this may still impact on measured isotopic values to some extent. However, no significant change of δ_T was observed during a 5-min chamber closure, which was attributed to the counteracting impacts of increased air temperature and relative humidity (Wang et al., 2012). Therefore, we believe that altered conditions inside the chamber had no significant overall impact on the three end members at our NPCE site. We suggest, though, that future studies can consider further detailed experimentation, necessary to quantify in full the impact of altered air temperature and humidity inside the chamber on measured isotopic values.

If water vapor condensed in the sampling line during transport from the chamber to the analyzer, a significant bias would be induced in measured isotopic values. Most daytime air temperatures ranged from 10 to 20 °C during our chamber measurements (data not shown), though daily mean was lower than 10 °C in some days (Figure 3). The precautions used in this study were twofold: (1) The sampling line was directly connected with a vaporizer heating up to 140 °C, and this prevented water vapor condensation before entering the vaporizer and analyzer; (2) the reduced sampling duration, as discussed above, lowered the probability of condensation. However, these two arrangements cannot fully guarantee that no condensation occurred in the sampling line during the measurement. Direct heating of the sampling line provides the best overall solution, and we recommend this for future experiments.

For the Keeling-CG method, the contributions made by input parameters to both T/ET and to δ_E itself were quantified (Figure 10b). The contribution of δ_{ET} to T/ET was 66.5%, similar to that of chamber method, and ~33% for δ_E and δ_T combined. This meant that the uncertainty in the T/ET ratio stemmed principally from the δ_{ET} value, that is, the Keeling plot. Many studies have discussed the sources of uncertainty and error inherent in Keeling plots (Good et al., 2012; Nickerson & Risk, 2009; Pataki et al., 2003; Wei et al., 2015). Pataki et al. (2003) and Good et al. (2012) proposed that the Keeling plot uncertainty could be reduced by increasing the sample size and the variability of vapor concentrations. Therefore, vapor concentrations and δ_V were measured at five heights in this study and the average uncertainty of Keeling plot was 1.1‰ for δ^{18}O. For δ_E, contributions were mainly made by δ_S and δ_V, accounting for 5.1% and 4.6%, respectively, of variation ("Flyout" of Figure 10b). The precise determination of the depth of the evaporating front was critical because δ_S varied considerably near the evaporating front. Hence, the failure to determine the evaporating front may produce a large bias within the δ_E data (Dubbert et al., 2013). The evaporating front is usually clearly identified by the enrichment of heavy isotopes in the vertical soil water isotope profile. Using observations of soil water isotope profile has therefore been conventionally treated as a reasonable way to determine the depth of the evaporating front (Dubbert et al., 2013; Sutanto et al., 2014). In this study, the isotopic compositions of soil water at a range of depths (Figure S4) imply that the evaporating front is at 20 cm. The use of other depth of soil water isotope may induce a maximum T/ET bias of 0.20.

Looking ahead to potential future analyses, the recently developed continuous soil water isotope monitoring system may improve the precise determination of the evaporating front (Rothfuss et al., 2015). However, although kinetic fractionation factor ε_K contributed to 12.5% of the change of δ_E, its impact on T/ET was small (1.4%) due to the low contribution (11.2%) of δ_E to T/ET (Figure 10b). Previous studies have

suggested that the ISS was achieved by midday and/or early afternoon or over a long-term timescale (Lai et al., 2006; Welp et al., 2008; Yakir & Wang, 1996). This assumption has been confirmed by recent observations (Hu et al., 2014; Wei et al., 2015; Wen et al., 2016; Xiao et al., 2012). At midday and in the early afternoon, transpiration from plants is usually at its highest, having a short turnover time of leaf water, and thus constrains δ_T close to the isotopic composition of plant source water (Wen et al., 2016). Moreover, the low canopy height and short leaf (low leaf water content) in our study facilitated the attainment of an ISS (Wang et al., 2015; Yakir & Wang, 1996). Therefore, we suggested that an ISS was a reasonable assumption in our observations during the month of July in 2014.

Evaporation from canopy interception was not included in ET for both the chamber and Keeling-CG methods, as isotopic observations were conducted typically during the no-rain periods. However, interception (dew or preceding rain) may even present in no-rain period and bias the values of δ_T and δ_{ET}. Measurements conducted in this condition should be excluded and not involved in T/ET calculation. On rainy days, interception evaporation may constitute a significant part of ET, although this phenomenon is more evident in regions with dense vegetation cover (e.g., tropical vegetation; Miralles et al., 2010; Wei et al., 2017). Hence, our calculated T/ET may be, to some extent, overestimated (when compared to long-term means) due to the lack of interception evaporation after precipitation.

5. Conclusions

By using newly developed high-frequency laser spectrometer and customized chambers, we partitioned ET into E and T for an alpine meadow ecosystem in the central TP. At the seasonal timescale, δ_{ET}, δ_E, and δ_T showed consistent variations and were all related to the precipitation isotope. We found that T/ET ranged from 0.40 to 0.73, with an average value of 0.43. These values were additionally supported by T/ET values derived, independently, from a two-source model and EC observation. T/ET was correlated with θ at the seasonal timescale, in addition to LAI. Our main finding is that environmental conditions (here soil water content, θ) dominated T/ET change in arid and semiarid regions, with LAI playing a secondary role. This result sheds light on the additional mechanisms underlying the spatial pattern and temporal change of terrestrial transpiration and will aid the calibration of land-surface models for use in full climate simulations. Our measurement framework provides new ways to investigate large-scale T/ET behaviors in arid and semiarid regions, and can inform modeling and related studies of regional or global water cycles, by better representation of mechanisms controlling transpiration within the land surface.

Appendix A: *ET* Partitioning Based on a Two-Source Model

The partitioning of ET into canopy (T) and soil components (E) was performed based on EC measurements ET and a two-source model following (Wang & Yamanaka, 2014). Assuming that the energy of photosynthesis and that induced by advection are negligible, then the radiation/energy balance equations in the vegetation canopy and at the ground surface can be expressed as

$$R_{nV} = (1 - f_V)\left[(1 - \alpha_V)S_d + L_d + \sigma T_G^4 - 2\sigma T_L^4\right] = H_V + lT \tag{A1}$$

$$R_{nG} = f_V[(1 - \alpha_G)S_d + L_d] + (1 - f_V)\sigma T_L^4 - \sigma T_G^4] = G + H_G + lE \tag{A2}$$

where R_{nV} and R_{nG} are the net radiation of vegetation canopy and at the ground surface (W/m^2), H_V and H_G are the sensible heat flux from the vegetation canopy and ground surface (W/m^2), f_v is the permittivity of the vegetation canopy, α_V and α_G are albedos of vegetation canopy and ground surface, S_d and L_d are downward shortwave and longwave radiation (W/m^2), σ is the Stefan-Boltzmann constant ($=5.67 \times 10^{-8}$ W $\cdot$ m^{-2} $\cdot$ K^{-4}), l is the latent heat of vaporization (J/kg), T_G and T_L are ground surface and leaf temperature (°C), G is ground heat flux (W/m^2), and H_G is sensible heat flux from ground surface (W/m^2). The total flux per unit area is given as the sum of the vegetation canopy and ground surface, that is, $R_n = R_{nV} + R_{nG}$, $H = H_V + H_G$, and $lET = l(E + T)$. f_V was given as a function of LAI as follows:

$$f_V = 1\text{-}\tanh(c_{LAI}\mathrm{LAI}) \tag{A3}$$

where c_{LAI} is empirical constant and assumed to be unity in this study. α_V and α_G are assumed to be constant as 0.2 and 0.1, respectively.

When all these driver and estimates are combined to force the two-source model, the T and E fluxes can be calculated as

$$T = \rho_a[q_{\text{sat}}(T_L) - q_a]/(r_{aV} + r_c) \tag{A4}$$

$$E = \rho_a[q_{\text{sat}}(T_G) - q_a]/(r_{aG} + r_{ss}) \tag{A5}$$

where $q_{\text{sat}}(T_L)$ and $q_{\text{sat}}(T_G)$ are saturated specific humidity for temperature of leaf and ground surface (kg/kg); q_{a} is air specific humidity (kg/kg) as a function of T_a, h_a, and air pressure (P); r_{aV} and r_{aG} are aerodynamic resistance for vegetation canopy and ground surface (s/m); and r_c and r_{ss} are canopy (stomatal) resistance and surface soil resistance (s/m). Variable r_{c} is given as

$$r_c = r_{st}/\text{LAI} \tag{A6}$$

where r_{st} is leaf stomatal resistance and can be calculated as

$$r_{st} = \frac{r_{st\_\min}}{c_{sw}} + \frac{r_{st\_\max} - r_{st\_\min}}{c_{sw}}\left\{1 - \tanh\left(\frac{S_d}{c_{sd}}\right)\right\} \tag{A7}$$

where $r_{st\_\min}$ and $r_{st\_\max}$ are minimum and maximum values of leaf stomatal resistance (s/m) when soil is sufficiently wet. These parameters are regarded as tunable, and so they are set as 100 and 10,000 by the trial-and-error method so as to minimize the difference between predicted and measured energy fluxes. Similarly, $c_{sw} = \theta/\theta_{\max}$, θ is volumetric soil water content (m^3/m^3) and $\theta_{\max} = 0.35\ m^3/m^3$ is the maximum water content during observational period, and $c_{sd} = 25\ W/m^2$. Variable r_{ss} is given as a function of θ:

$$r_{ss} = a(\theta_s/\theta)^b + c \tag{A8}$$

where θ_{s} is saturated water content (m^3/m^3) and empirical constants a, b, and c are derived by optimization mentioned earlier and set as 3.5, 2.3, and 433.4, respectively. Variable r_{aV} and r_{aG} can be calculated as follows:

$$r_{aV} = \ln\left(\frac{z_m - d_0}{z_{0mV}}\right)\ln\left(\frac{z_h - d_0}{z_{0hV}}\right)/k^2u \tag{A9}$$

$$r_{aG} = \ln\left(\frac{z_m}{z_{0mG}}\right)\ln\left(\frac{z_h}{z_{0hG}}\right)/k^2u \tag{A10}$$

where z_m is height of wind speed measurement (m), z_h is height of temperature and humidity measurements, d_0 ($= 0.666z_V$; z_V is vegetation height in m) is the zero-plane displacement height (m), z_{0mV} ($= 0.123\ z_{\text{V}}$) and z_{0hV} ($= 0.1z_{0\text{mV}}$) are roughness length governing momentum and heat (and vapor) transfer above vegetation canopy (m), k is the von Karman's constant ($= 0.41$), and u is wind speed (m/s). Quantities z_{0mG} ($= 10^{-4}$) and z_{0hG} ($= 0.1z_{0\text{mG}}$) are roughness length governing momentum and heat (and vapor) transfer above ground surface (m).

Using input parameters and equations (A1)–(A10), and the EC-derived ET, this allows T and E to be calculated and thus the T/ET ratio at hourly scale. Results with rainy period were removed. These T/ET estimates were then compared against the daily average T/ET values calculated during period 8:00–18:00 and based on our isotope measurements (Figure 5).

Acknowledgments
This research was funded by National Natural Science Foundation of China (grants 41771043, 41530748, and 41801047). The meteorological data were provided by Nagqu Station of Plateau Climate and Environment, Chinese of Academy of Sciences. C. H. was supported by the Natural Environment Research Council award NE/R016429/1 as part of the UK-SCAPE program delivering National Capability. C. H. was also supported by the Newton Fund, Climate Science for Service Partnership China (CSSP-China). Data used in this study are available on repository (https://figshare.com/articles/Nagqu_data/10008929).

References

Aemisegger, F., Sturm, P., Graf, P., Sodemann, H., Pfahl, S., Knohl, A., & Wernli, H. (2012). Measuring variations of $\delta^{18}O$ and $\delta^{2}H$ in atmospheric water vapour using two commercial laser-based spectrometers: An instrument characterisation study. *Atmospheric Measurement Techniques*, *5*(7), 1491–1511. https://doi.org/10.5194/amt-5-1491-2012

Berkelhammer, M., Noone, D. C., Wong, T. E., Burns, S. P., Knowles, J. F., Kaushik, A., et al. (2016). Convergent approaches to determine an ecosystem's transpiration fraction. *Global Biogeochemical Cycles*, *30*, 933–951. https://doi.org/10.1002/2016GB005392

Bréda, N. J. (2003). Ground-based measurements of leaf area index: A review of methods, instruments and current controversies. *Journal of Experimental Botany*, *54*(392), 2403–2417. https://doi.org/10.1093/jxb/erg263

Cappa, C. D., Hendricks, M. B., DePaolo, D. J., & Cohen, R. C. (2003). Isotopic fractionation of water during evaporation. *Journal of Geophysical Research*, *108*(D16), 4525. https://doi.org/10.1029/2003JD003597

Chen, Y., Yang, K., Tang, W., Qin, J., & Zhao, L. (2012). Parameterizing soil organic carbon's impacts on soil porosity and thermal parameters for Eastern Tibet grasslands. *Science China Earth Sciences*, *55*(6), 1001–1011. https://doi.org/10.1007/s11430-012-4433-0

Craig, H., & Gordon, L. I. (1965). Deuterium and oxygen 18 variations in the ocean and the marine atmosphere. In E. Tongiorgi (Ed.), *Stable isotope in oceanic studies and paleotemperatures*, (pp. 9–130). Varenna: Lab. Di Geol. Nucl.

Cui, J., Tian, L., Biggs, T. W., & Wen, R. (2017). Deuterium-excess determination of evaporation to inflow ratios of an alpine lake: Implications for water balance and modeling. *Hydrological Processes*, *31*(5), 1034–1046. https://doi.org/10.1002/hyp.11085

Cui, J., Tian, L., Gerlein-Safdi, C., & Qu, D. (2017). The influence of memory, sample size effects, and filter paper material on online laser-based plant and soil water isotope measurements. *Rapid Communications in Mass Spectrometry*, *31*(6), 509–522. https://doi.org/10.1002/rcm.7824

Dubbert, M., Cuntz, M., Piayda, A., Maguás, C., & Werner, C. (2013). Partitioning evapotranspiration—Testing the Craig and Gordon model with field measurements of oxygen isotope ratios of evaporative fluxes. *Journal of Hydrology*, *496*, 142–153.

Dubbert, M., Cuntz, M., Piayda, A., & Werner, C. (2014). Oxygen isotope signatures of transpired water vapor: The role of isotopic non-steady-state transpiration under natural conditions. *The New Phytologist*, *203*(4), 1242–1252. https://doi.org/10.1111/nph.12878

Farquhar, G. D., & Cernusak, L. A. (2005). On the isotopic composition of leaf water in the non-steady state. *Functional Plant Biology*, *32*(4), 293–303. https://doi.org/10.1071/fp04232

Good, S. P., Noone, D., & Bowen, G. (2015). Hydrologic connectivity constrains partitioning of global terrestrial water fluxes. *Science*, *349*(6244), 175–177. https://doi.org/10.1126/science.aaa5931

Good, S. P., Soderberg, K., Guan, K., King, E. G., Scanlon, T. M., & Caylor, K. K. (2014). δ^2H isotopic flux partitioning of evapotranspiration over a grass field following a water pulse and subsequent dry down. *Water Resources Research*, *50*, 1410–1432. https://doi.org/10.1002/2013WR014333

Good, S. P., Soderberg, K., Wang, L., & Caylor, K. K. (2012). Uncertainties in the assessment of the isotopic composition of surface fluxes: A direct comparison of techniques using laser-based water vapor isotope analyzers. *Journal of Geophysical Research*, *117*, D15301. https://doi.org/10.1029/2011JD017168

Groning, M., Lutz, H. O., Roller-Lutz, Z., Kralik, M., Gourcy, L., & Poltenstein, L. (2012). A simple rain collector preventing water re-evaporation dedicated for delta O-18 and delta H-2 analysis of cumulative precipitation samples. *Journal of Hydrology*, *448*, 195–200. https://doi.org/10.1016/j.jhydrol.2012.04.041

Guo, X., Tian, L., Wang, L., Yu, W., & Qu, D. (2017). River recharge sources and the partitioning of catchment evapotranspiration fluxes as revealed by stable isotope signals in a typical high-elevation arid catchment. *Journal of Hydrology*, *549*, 616–630. https://doi.org/10.1016/j.jhydrol.2017.04.037

Gupta, P., Noone, D., Galewsky, J., Sweeney, C., & Vaughn, B. H. (2009). Demonstration of high-precision continuous measurements of water vapor isotopologues in laboratory and remote field deployments using wavelength-scanned cavity ring-down spectroscopy (WS-CRDS) technology. *Rapid Communications in Mass Spectrometry*, *23*(16), 2534–2542. https://doi.org/10.1002/rcm.4100

Haverd, V., Cuntz, M., Griffith, D., Keitel, C., Tadros, C., & Twining, J. (2011). Measured deuterium in water vapour concentration does not improve the constraint on the partitioning of evapotranspiration in a tall forest canopy, as estimated using a soil vegetation atmosphere transfer model. *Agricultural and Forest Meteorology*, *151*(6), 645–654. https://doi.org/10.1016/j.agrformet.2011.02.005

Horita, J., Rozanski, K., & Cohen, S. (2008). Isotope effects in the evaporation of water: A status report of the Craig-Gordon model. *Isotopes in Environmental and Health Studies*, *44*(1), 23–49. https://doi.org/10.1080/10256010801887174

Horita, J., & Wesolowski, D. J. (1994). Liquid-vapor fractionation of oxygen and hydrogen isotopes of water from the freezing to the critical temperature. *Geochimica Et Cosmochimica Acta*, *58*(16), 3425–3437. https://doi.org/10.1016/0016-7037(94)90096-5

Hu, Z., Wen, X., Sun, X., Li, L., Yu, G., Lee, X., & Li, S. (2014). Partitioning of evapotranspiration through oxygen isotopic measurements of water pools and fluxes in a temperate grassland. *Journal of Geophysical Research*, *119*, 358–372. https://doi.org/10.1002/2013JG002367

Hu, Z., Yu, G., Fu, Y., Sun, X., Li, Y., Shi, P., et al. (2008). Effects of vegetation control on ecosystem water use efficiency within and among four grassland ecosystems in China. *Global Change Biology*, *14*(7), 1609–1619. https://doi.org/10.1111/j.1365-2486.2008.01582.x

Hu, Z., Yu, G., Zhou, Y., Sun, X., Li, Y., Shi, P., et al. (2009). Partitioning of evapotranspiration and its controls in four grassland ecosystems: Application of a two-source model. *Agricultural and Forest Meteorology*, *149*(9), 1410–1420. https://doi.org/10.1016/j.agrformet.2009.03.014

Jasechko, S., Sharp, Z. D., Gibson, J. J., Birks, S. J., Yi, Y., & Fawcett, P. J. (2013). Terrestrial water fluxes dominated by transpiration. *Nature*, *496*(7445), 347–350. https://doi.org/10.1038/nature11983

Keeling, C. D. (1958). The concentration and isotopic abundances of atmospheric carbon dioxide in rural areas. *Geochimica et Cosmochimica Acta*, *13*(4), 322–334. https://doi.org/10.1016/0016-7037(58)90033-4

Kool, D., Agam, N., Lazarovitch, N., Heitman, J. L., Sauer, T. J., & Ben-Gal, A. (2014). A review of approaches for evapotranspiration partitioning. *Agricultural and Forest Meteorology*, *184*, 56–70.

Lai, C. T., Ehleringer, J. R., Bond, B. J., & Paw, U. K. T. (2006). Contributions of evaporation, isotopic non-steady state transpiration and atmospheric mixing on the delta O-18 of water vapour in Pacific Northwest coniferous forests. *Plant, Cell & Environment*, *29*(1), 77–94. https://doi.org/10.1111/j.1365-3040.2005.01402.x

Lian, X., Piao, S., Huntingford, C., Li, Y., Zeng, Z., Wang, X., et al. (2018). Partitioning global land evapotranspiration using CMIP5 models constrained by observations. *Nature Climate Change*, *8*(7), 640–646. https://doi.org/10.1038/s41558-018-0207-9

Liu, C. M., Zhang, X. Y., & Zhang, Y. Q. (2002). Determination of daily evaporation and evapotranspiration of winter wheat and maize by large-scale weighing lysimeter and micro-lysimeter. *Agricultural and Forest Meteorology*, *111*(2), 109–120. https://doi.org/10.1016/s0168-1923(02)00015-1

Lu, X., Liang, L. L., Wang, L., Jenerette, G. D., McCabe, M. F., & Grantz, D. A. (2017). Partitioning of evapotranspiration using a stable isotope technique in an arid and high temperature agricultural production system. *Agricultural Water Management*, *179*, 103–109. https://doi.org/10.1016/j.agwat.2016.08.012

Ma, N., Niu, G.-Y., Xia, Y., Cai, X., Zhang, Y., Ma, Y., & Fang, Y. (2017). A systematic evaluation of Noah-MP in simulating land-atmosphere energy, water, and carbon exchanges over the continental United States. *Journal of Geophysical Research: Atmospheres*, *122*, 12,245–212,268. https://doi.org/10.1002/2017JD027597

Ma, N., Szilagyi, J., Zhang, Y., & Liu, W. (2019). Complementary-relationship-based modeling of terrestrial evapotranspiration across China during 1982–2012: Validations and spatiotemporal analyses. *Journal of Geophysical Research: Atmospheres*, *124*, 4326–4351. https://doi.org/10.1029/2018JD029850

Ma, N., Zhang, Y. S., Xu, C. Y., & Szilagyi, J. (2015). Modeling actual evapotranspiration with routine meteorological variables in the data-scarce region of the Tibetan Plateau: Comparisons and implications. *Journal of Geophysical Research: Biogeosciences*, *120*, 1638–1657. https://doi.org/10.1002/2015JG003006

Ma, W., & Ma, Y. (2019). The evaluation of AMSR-E soil moisture data in atmospheric modeling using a suitable time series iteration to derive land surface fluxes over the Tibetan Plateau. *PLoS ONE*, *14*(12), e0226373. https://doi.org/10.1371/journal.pone.0226373

Mathieu, R., & Bariac, T. (1996). A numerical model for the simulation of stable isotope profiles in drying soils. *Journal of Geophysical Research*, *101*(D7), 12685. https://doi.org/10.1029/96jd00223

Maxwell, R. M., & Condon, L. E. (2016). Connections between groundwater flow and transpiration partitioning. *Science*, *353*(6297), 377–380. https://doi.org/10.1126/science.aaf7891

Merlivat, L. (1978). Molecular diffusivities of $H_2{}^{16}O$, $HD^{16}O$ and $H_2{}^{18}O$ in gases. *The Journal of Chemical Physics*, *69*(6), 2864–2871.

Miralles, D. G., Gash, J. H., Holmes, T. R. H., de Jeu, R. A. M., & Dolman, A. J. (2010). Global canopy interception from satellite observations. *Journal of Geophysical Research*, *115*, D16122. https://doi.org/10.1029/2009JD013530

Miralles, D. G., Jiménez, C., Jung, M., Michel, D., Ershadi, A., McCabe, M. F., et al. (2016). The WACMOS-ET project—Part 2: Evaluation of global terrestrial evaporation data sets. *Hydrology and Earth System Sciences*, *20*(2), 823–842. https://doi.org/10.5194/hess-20-823-2016

Nickerson, N., & Risk, D. (2009). Keeling plots are non-linear in non-steady state diffusive environments. *Geophysical Research Letters*, *36*, L08401. https://doi.org/10.1029/2008GL036945

Pataki, D. E., Ehleringer, J. R., Flanagan, L. B., Yakir, D., Bowling, D. R., Still, C. J., et al. (2003). The application and interpretation of Keeling plots in terrestrial carbon cycle research. *Global Biogeochemical Cycles*, *17*(1), 1022. https://doi.org/10.1029/2001GB001850

Rigden, A. J., Salvucci, G. D., Entekhabi, D., & Short Gianotti, D. J. (2018). Partitioning evapotranspiration over the continental United States using weather Station data. *Geophysical Research Letters*, *45*, 9605–9613. https://doi.org/10.1029/2018GL079121

Rothfuss, Y., Biron, P., Braud, I., Canale, L., Durand, J. L., Gaudet, J. P., et al. (2010). Partitioning evapotranspiration fluxes into soil evaporation and plant transpiration using water stable isotopes under controlled conditions. *Hydrological Processes*, *24*(22), 3177–3194.

Rothfuss, Y., Merz, S., Vanderborght, J., Hermes, N., Weuthen, A., Pohlmeier, A., et al. (2015). Long-term and high-frequency non-destructive monitoring of water stable isotope profiles in an evaporating soil column. *Hydrology and Earth System Sciences*, *19*(10), 4067–4080. https://doi.org/10.5194/hess-19-4067-2015

Schlesinger, W. H., & Jasechko, S. (2014). Transpiration in the global water cycle. *Agricultural and Forest Meteorology*, *189-190*, 115–117. https://doi.org/10.1016/j.agrformet.2014.01.011

Steen-Larsen, H. C., Johnsen, S. J., Masson-Delmotte, V., Stenni, B., Risi, C., Sodemann, H., et al. (2013). Continuous monitoring of summer surface water vapor isotopic composition above the Greenland Ice Sheet. *Atmospheric Chemistry and Physics*, *13*(9), 4815–4828. https://doi.org/10.5194/acp-13-4815-2013

Sun, S., Meng, P., Zhang, J., Wan, X., Zheng, N., & He, C. (2014). Partitioning oak woodland evapotranspiration in the rocky mountainous area of North China was disturbed by foreign vapor, as estimated based on non-steady-state 18O isotopic composition. *Agricultural and Forest Meteorology*, *184*, 36–47. https://doi.org/10.1016/j.agrformet.2013.08.006

Sun, X., Wilcox, B. P., & Zou, C. B. (2019). Evapotranspiration partitioning in dryland ecosystems: A global meta-analysis of in situ studies. *Journal of Hydrology*, *576*, 123–136. https://doi.org/10.1016/j.jhydrol.2019.06.022

Sutanto, S. J., van den Hurk, B., Dirmeyer, P. A., Seneviratne, S. I., Röckmann, T., Trenberth, K. E., et al. (2014). HESS opinions "A perspective on isotope versus non-isotope approaches to determine the contribution of transpiration to total evaporation". *Hydrology and Earth System Sciences*, *18*(8), 2815–2827. https://doi.org/10.5194/hess-18-2815-2014

Sutanto, S. J., Wenninger, J., Coenders-Gerrits, A. M. J., & Uhlenbrook, S. (2012). Partitioning of evaporation into transpiration, soil evaporation and interception: A comparison between isotope measurements and a HYDRUS-1D model. *Hydrology and Earth System Sciences*, *16*(8), 2605–2616. https://doi.org/10.5194/hess-16-2605-2012

Tian, L., Yao, T., MacClune, K., White, J. W. C., Schilla, A., Vaughn, B., et al. (2007). Stable isotopic variations in west China: A consideration of moisture sources. *Journal of Geophysical Research*, *112*, D10112. https://doi.org/10.1029/2006JD007718

Volkmann, T. H., Haberer, K., Gessler, A., & Weiler, M. (2016). High-resolution isotope measurements resolve rapid ecohydrological dynamics at the soil-plant interface. *The New Phytologist*, *210*(3), 839–849. https://doi.org/10.1111/nph.13868

Wang, K., & Dickinson, R. E. (2012). A review of global terrestrial evapotranspiration: Observation, modeling, climatology, and climatic variability. *Reviews of Geophysics*, *50*, RG2005. https://doi.org/10.1029/2011RG000373

Wang, L., Caylor, K. K., Villegas, J. C., Barron-Gafford, G. A., Breshears, D. D., & Huxman, T. E. (2010). Partitioning evapotranspiration across gradients of woody plant cover: Assessment of a stable isotope technique. *Geophysical Research Letters*, *37*, L09401. https://doi.org/10.1029/2010GL043228

Wang, L., Good, S. P., & Caylor, K. K. (2014). Global synthesis of vegetation control on evapotranspiration partitioning. *Geophysical Research Letters*, *41*, 6753–6757. https://doi.org/10.1002/2014GL061439

Wang, L., Good, S. P., Caylor, K. K., & Cernusak, L. A. (2012). Direct quantification of leaf transpiration isotopic composition. *Agricultural and Forest Meteorology*, *154-155*, 127–135. https://doi.org/10.1016/j.agrformet.2011.10.018

Wang, L. X., Niu, S. L., Good, S. P., Soderberg, K., McCabe, M. F., Sherry, R. A., et al. (2013). The effect of warming on grassland evapotranspiration partitioning using laser-based isotope monitoring techniques. *Geochimica et Cosmochimica Acta*, *111*, 28–38. https://doi.org/10.1016/j.gca.2012.12.047

Wang, P., Li, X.-Y., Huang, Y., Liu, S., Xu, Z., Wu, X., & Ma, Y.-J. (2016). Numerical modeling the isotopic composition of evapotranspiration in an arid artificial oasis cropland ecosystem with high-frequency water vapor isotope measurement. *Agricultural and Forest Meteorology*, *230-231*, 79–88. https://doi.org/10.1016/j.agrformet.2015.12.063

Wang, P., Li, X. Y., Wang, L., Wu, X., Hu, X., Fan, Y., & Tong, Y. (2018). Divergent evapotranspiration partition dynamics between shrubs and grasses in a shrub-encroached steppe ecosystem. *The New Phytologist*, *219*(4), 1325–1337. https://doi.org/10.1111/nph.15237

Wang, P., & Yamanaka, T. (2014). Application of a two-source model for partitioning evapotranspiration and assessing its controls in temperate grasslands in central Japan. *Ecohydrology*, *7*(2), 345–353. https://doi.org/10.1002/eco.1352

Wang, P., Yamanaka, T., Li, X.-Y., & Wei, Z. (2015). Partitioning evapotranspiration in a temperate grassland ecosystem: Numerical modeling with isotopic tracers. *Agricultural and Forest Meteorology*, *208*, 16–31. https://doi.org/10.1016/j.agrformet.2015.04.006

Wei, Z., Lee, X., Wen, X., & Xiao, W. (2018). Evapotranspiration partitioning for three agro-ecosystems with contrasting moisture conditions: A comparison of an isotope method and a two-source model calculation. *Agricultural and Forest Meteorology*, *252*, 296–310. https://doi.org/10.1016/j.agrformet.2018.01.019

Wei, Z., Yoshimura, K., Okazaki, A., Kim, W., Liu, Z., & Yokoi, M. (2015). Partitioning of evapotranspiration using high-frequency water vapor isotopic measurement over a rice paddy field. *Water Resources Research*, *51*, 3716–3729. https://doi.org/10.1002/2014WR016737

Wei, Z., Yoshimura, K., Wang, L., Miralles, D. G., Jasechko, S., & Lee, X. (2017). Revisiting the contribution of transpiration to global terrestrial evapotranspiration. *Geophysical Research Letters*, *44*, 2792–2801. https://doi.org/10.1002/2016GL072235

Welp, L. R., Lee, X., Kim, K., Griffis, T. J., Billmark, K. A., & Baker, J. M. (2008). $\delta^{18}O$ of water vapour, evapotranspiration and the sites of leaf water evaporation in a soybean canopy. *Plant, Cell & Environment*, *31*(9), 1214–1228.

Wen, X., Yang, B., Sun, X., & Lee, X. (2016). Evapotranspiration partitioning through in-situ oxygen isotope measurements in an oasis cropland. *Agricultural and Forest Meteorology*, *230-231*, 89–96. https://doi.org/10.1016/j.agrformet.2015.12.003

Williams, D., Cable, W., Hultine, K., Hoedjes, J., Yepez, E., Simonneaux, V., et al. (2004). Evapotranspiration components determined by stable isotope, sap flow and eddy covariance techniques. *Agricultural and Forest Meteorology*, *125*(3), 241–258.

Wu, Y., Du, T., Ding, R., Tong, L., Li, S., & Wang, L. (2016). Multiple methods to partition evapotranspiration in a maize field. *Journal of Hydrometeorology*. https://doi.org/10.1175/jhm-d-16-0138.1

Xiao, W., Lee, X., Wen, X., Sun, X., & Zhang, S. (2012). Modeling biophysical controls on canopy foliage water ^{18}O enrichment in wheat and corn. *Global Change Biology*, *18*(5), 1769–1780. https://doi.org/10.1111/j.1365-2486.2012.02648.x

Xiao, W., Wei, Z., & Wen, X. (2018). Evapotranspiration partitioning at the ecosystem scale using the stable isotope method—A review. *Agricultural and Forest Meteorology*, *263*, 346–361. https://doi.org/10.1016/j.agrformet.2018.09.005

Xue, B. L., Wang, L., Yang, K., Tian, L. D., Qin, J., Chen, Y. Y., et al. (2013). Modeling the land surface water and energy cycles of a mesoscale watershed in the central Tibetan Plateau during summer with a distributed hydrological model. *Journal of Geophysical Research: Atmospheres*, *118*, 8857–8868. https://doi.org/10.1002/jgrd.50696

Yakir, D., & Sternberg, L. D. L. (2000). The use of stable isotopes to study ecosystem gas exchange. *Oecologia*, *123*(3), 297–311. https://doi.org/10.1007/s004420051016

Yakir, D., & Wang, X.-F. (1996). Fluxes of CO_2 and water between terrestrial vegetation and the atmosphere estimated from isotope measurements. *Nature*, *380*, 515–517. https://doi.org/10.1038/380515a0

Yan, K., Park, T., Yan, G., Liu, Z., Yang, B., Chen, C., et al. (2016). Evaluation of MODIS LAI/FPAR Product Collection 6. Part 2: Validation and Intercomparison. *Remote Sensing*, *8*(6). https://doi.org/10.3390/rs8060460

Yang, K., Qin, J., Zhao, L., Chen, Y., Tang, W., Han, M., et al. (2013). A multiscale soil moisture and freeze–thaw monitoring network on the third pole. *Bulletin of the American Meteorological Society*, *94*(12), 1907–1916. https://doi.org/10.1175/bams-d-12-00203.1

Yang, K., Ye, B. S., Zhou, D. G., Wu, B. Y., Foken, T., Qin, J., & Zhou, Z. Y. (2011). Response of hydrological cycle to recent climate changes in the Tibetan Plateau. *Climatic Change*, *109*(3–4), 517–534. https://doi.org/10.1007/s10584-011-0099-4

Yao, T., Masson-Delmotte, V., Gao, J., Yu, W., Yang, X., Risi, C., et al. (2013). A review of climatic controls on δ18O in precipitation over the Tibetan Plateau: Observations and simulations. *Reviews of Geophysics*, *51*, 525–548. https://doi.org/10.1002/rog.20023

Yepez, E. A., Williams, D. G., Scott, R. L., & Lin, G. (2003). Partitioning overstory and understory evapotranspiration in a semiarid savanna woodland from the isotopic composition of water vapor. *Agricultural and Forest Meteorology*, *119*(1), 53–68.

Zhang, Y., Pena-Arancibia, J. L., McVicar, T. R., Chiew, F. H., Vaze, J., Liu, C., et al. (2016). Multi-decadal trends in global terrestrial evapotranspiration and its components. *Scientific Reports*, *6*, 19,124. https://doi.org/10.1038/srep19124